# Chapter 6
# Shock Wave Mitigation


## 6.1 Introduction

Shock wave mitigation in air is one of the important research topics of the shock-wave research. Strong or moderate shock waves can be attenuated in a relatively straightforward manner, whereas weak shock waves take a longer process to be attenuated to sound waves. In this chapter experimental results of shock wave mitigations are presented.

## 6.2 Suppression of Automobile Engine Exhaust Gas Noise

The suppression of automobile engine exhaust noises (Sekine et al. 1989) and the suppression of train tunnel sonic booms (Sasoh et al. 1998) were interesting applications of shock wave research.

Matsumura visualized pressure waves built up along an exhaust gas pipe line connected to a 500 cc Subaru automobile engine operated at 2000 rpm. Gases discharged from the cylinder having high pressure and temperatures coalesced during their propagation, into weak shock waves and then entered into the manifold. Recorded overpressures in exhaust gases are about 20 kPa and the specific heats ratio of exhaust gas mixtures of air and combustion product gases and debris is 1.35; therefore, the shock wave Mach number, Ms, appearing in the exhaust pipe flow would be 1.1. This value is no longer considered as an acoustic wave but a weak shock wave. Car silencers are designed to suppress these waves were traditionally based on the acoustic theory. However, the acoustic theory would not be an appropriate approach for attenuating shock waves in the silencers.

In experiments aimed at suppressing exhaust gas pressure the 28 mm diameter exhaust pipe line of a half litter Subaru engine cylinder was connected to a 30 mm $\times$ 30 mm shock tube and a 40 mm $\times$ 80 mm shock section. The engine was operated at various rotation speeds. Sequential visualizations were conducted.



K. Takayama, *Visualization of Shock Wave Phenomena*,
https://doi.org/10.1007/978-3-030-19451-2_6

At that time, the engine rotation was synchronized with a Q-switch ruby laser irradiation. The motion of shock waves in the test section was sequentially visualized.

Figure 6.1 show holographic observation of a shock wave entering in the 40 mm × 80 mm shock tube test section. Twin vortices were generated at the corner, see Fig. 6.1a. In Fig. 6.1b–d, the transmitted shock wave propagated inside the test section and reflected from the upper and lower walls. Splashes composed of water vapors and debris contained in the exhaust gases covered the observation window glasses. The sequential images shown in Fig. 6.1 roughly simulate the condition in a real automobile engine manifold. Shapes of wall surface, wall conditions and partitions tested in the laboratory were helpful in acquisition of design data for practical silencers and mufflers (Matsumura 1995).

Compression waves in the exhaust gases coalesced into shock waves and were collected in the manifold. Then shock wave propagations in a manifold were visualized using two types of 2-D manifolds which modelled two half litter cylinders as shown in Fig. 6.2. The 2-D manifolds were sandwiched with two thick acrylic plates. In this analogue experiment, the engine produced shock waves having a strength of about Ms = 1.1 were produced by ignitions of 10 mg $AgN_3$ pellets which were confined in a space connected to the entry port and were sealed with a 9 μm thick Mylar diaphragm. For simulating an engine rotation speed of 2200 rpm by detonating explosives at frequency of about 13 ms interval.

Based on experimental data, the silence and mufflers of Subaru Legacy in 1993 version was designed. This was the first successful application of shock tube experiments for a practical automobile design. Today, prototype silencers and mufflers were designed numerically using a fine simulation scheme. The schemes were once quantitatively validated by comparing its predictions with the interferometric images.

## 6.3 Train Tunnel Sonic Boom

Japan is a mountainous country and then Japanese high-speed train network system has many short and long train tunnels. When a high speed train enters into a long tunnel, compression waves are built up ahead of the train. As the blockage ratio of the train cross section to the tunnel cross section is about 25%, the trains serve as a high speed piston having its blockage ratio of 25%; thereby producing trains of compression waves propagating at a sonic speed inside the tunnels. When the compression waves were released from the tunnel exit, train tunnel sonic blooms will startle people living in the vicinity of such long train tunnels. Then the train tunnel booms prevent complying the national demand to increase the train speed. For overcoming this problem, a collaborated research with the East Japan Railway Company was initiated aimed at mitigating train tunnel booms.

Figure 6.3a shows a 1:250 scale tunnel sonic boom simulator installed in the Shock Wave Research Center of the Institute of Fluid Science, Tohoku University.

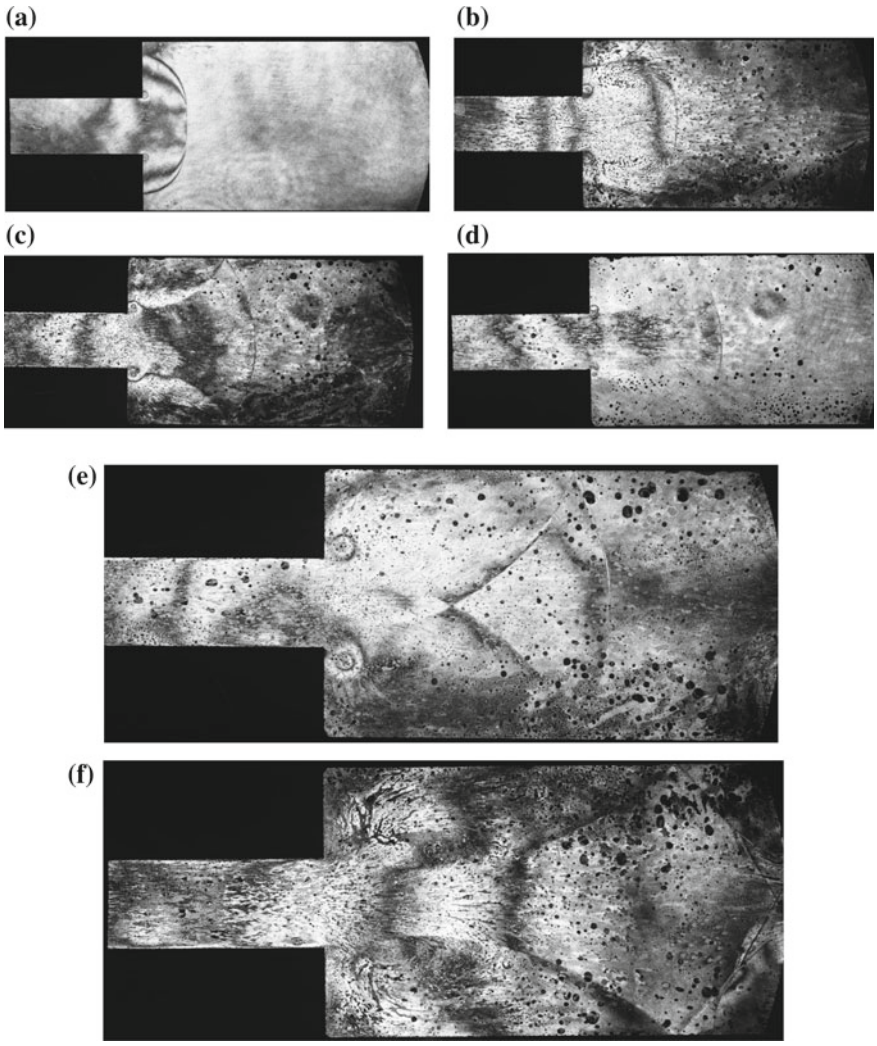


**Fig. 6.1** Shock waves generated in the exhaust gas pipe line of a Subaru engine: **a** #87042808, engine rotation 6800 rpm; **b** #87042809, 6800 rpm; **c** #87042806, 5900 rpm; **d** #87042807, 5899 rpm; **e** #87042810, 6500 rpm; **f** #87042812, 7500 rpm (Sekine et al. 1989)

The simulator consisted of, in principle, a $\phi$ 40 mm and it is about 20 m long steel tube tilted by 8°. It has a piston launcher, and its recovery system at the tube's end. The piston was a flat head cylinder composed of polycarbonate. It had 20 mm diameter and 200 mm long. Its blockage ratio to the simulator's cross section was 26% which was nearly identical with the real train/tunnel blockage ratio.

The piston was supported by a sabot at its front end and the rear end was accelerated by high pressure nitrogen as shown in Fig. 6.3b. Upon its impact against a tapered entry, the frontal sabot split into four pieces and the piston pass

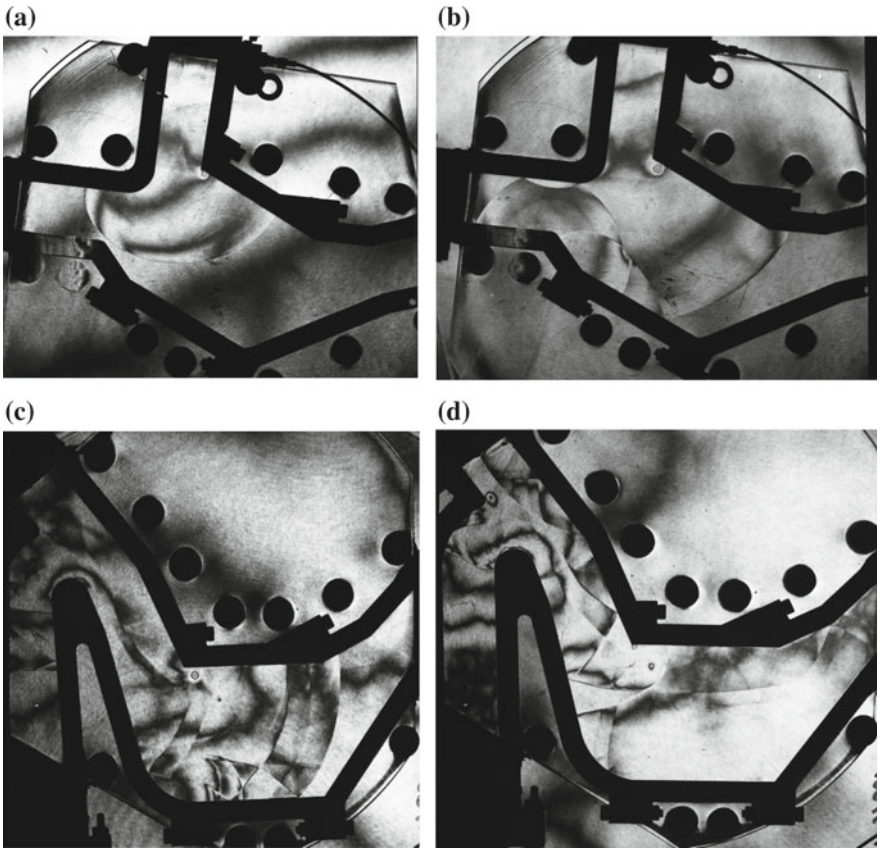


**Fig. 6.2** Shock wave mitigation in two-dimensional manifolds for Ms = 1.1 generated by the ignition of a 10 mg $AgN_3$ pellet: **a** #94110903; **b** #94110905; **c** #94111114; **d** #94111110 (Sekine et al. 1989)

thorough the hole. A rear sabot was, with propagation, plugged into the tapered entry hole and stopped the high pressure nitrogen to flow into the tunnel simulator. By adjusting the pressure in the driver chamber, it was possible to precisely control a piston speed from 50 to 120 m/s, equivalent to the train speed of from 189 to about 430 km/h. The piston moved along an open section of about 1 m long and hence compression waves built up in front of the piston was attenuated prior to its entry to the test section.

Figure 6.4a, b show the pressure history formed in front of the moving piston. The pressures were measured by distributed pressure transducers along the test section at the piston entry speed of 60 and 100 m/s, respectively. In Fig. 6.4a, the amplitudes of overpressures gradually decrease with the piston propagation.

For examining the effect of wall perforation on mitigation of train tunnel sonic booms, the wall surface was covered with a 5 mm thick perforated aluminum wall, which is, in short, a roughed wall test section consisting of porous aluminum plate.

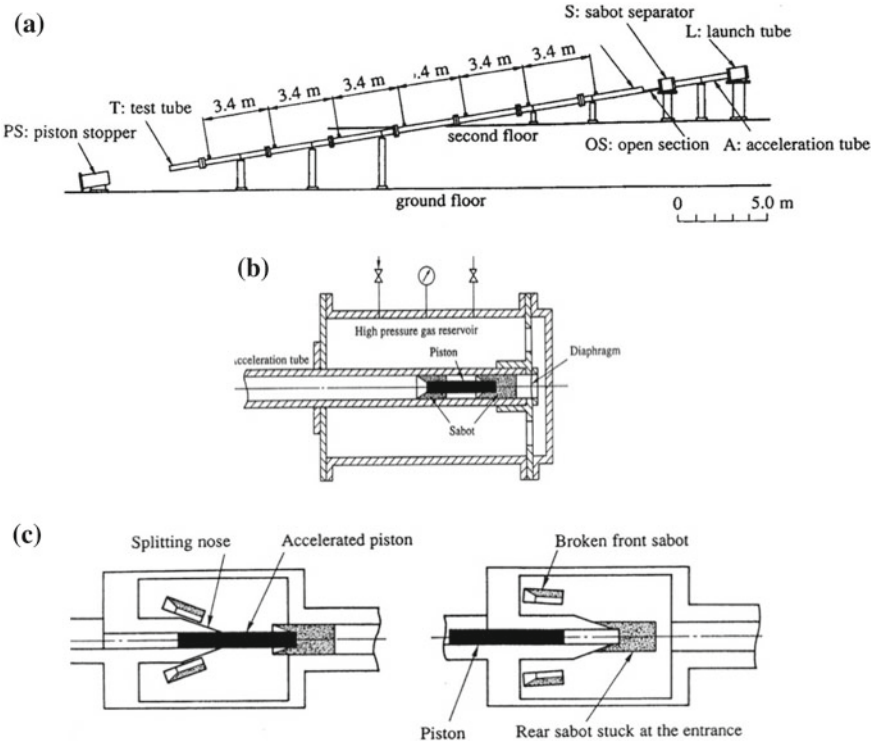


**Fig. 6.3** Tunnel simulator: **a** tunnel simulator; **b** launching setup; **c** piston release and recovery

Pressure transducers were distributed at every 0.2 m intervals along the perforated wall. Figure 6.5a shows a perforated wall. The wall in the absence of the wall perforation is defined as b = 0. The wall 16% of surface area is covered by two 10 mm wide and 5 mm seep porous aluminum plates is defined as b = 1.0. Figure 6.5b show the effect of wall perforations on the shock wave mitigation for B = 0, smooth wall and b = 0.16 and b = 1.0.

Assuming that the Mach number of the sonic boom is $Ms = 1 + \varepsilon$, $\varepsilon \ll 1$, the dimensionless overpressure of the boom $\Delta p$, can be related to $\varepsilon$, $\Delta p \sim (\gamma + 1)\varepsilon/4\gamma$, where $\gamma$ is the specific heats ratio and $\gamma = 1.4$ in air. In Fig. 6.5b, for instance, at x = 23.8 m, $\Delta p = 0.05$ and hence $\varepsilon = 0.02$. In Fig. 6.5b, the high speed entry of the flat head piston created a weak shock wave of Ms = 1.02 at x = 10.2 m. A negative pressure profile is observed at a distance of x = 3.4 m indicates the existence of expansion wave caused at the rear end of the piston causing recovery to the ambient pressure during its propagation. In Fig. 6.5b, the experimental results are summarized. The ordinate denotes the maximum pressure $\Delta p_{max}$ in kPa and the abscissa denotes the entry speed of a piston $u_p$ in m/s. Filled circles denote smooth wall, in other word, no coverage of roughened wall or b = 0, open circles denote 16% coverage or b = 0.16, and filled squares denote 100% coverage with perforation

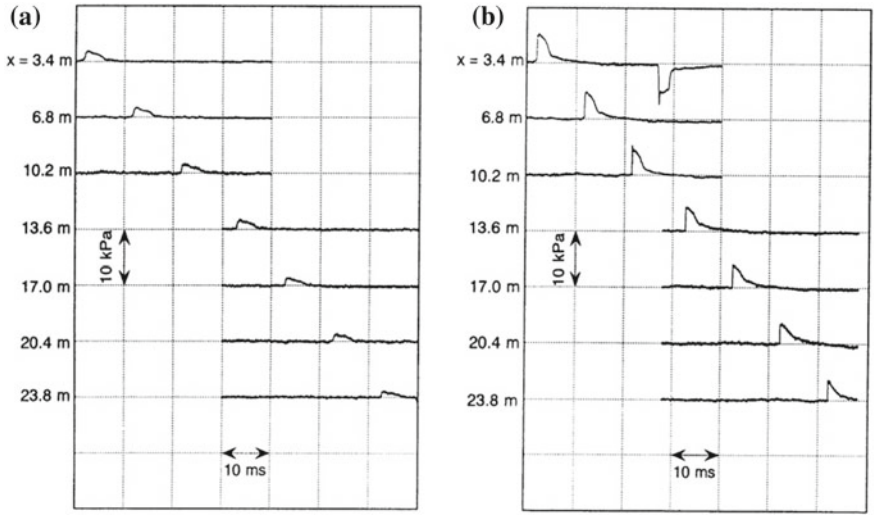


**Fig. 6.4** Formation of shock wave driven by a flat head piston: **a** piston speed 60 m/s or 216 km/h; **b** piston speed of 100 m/s or 360 km/h

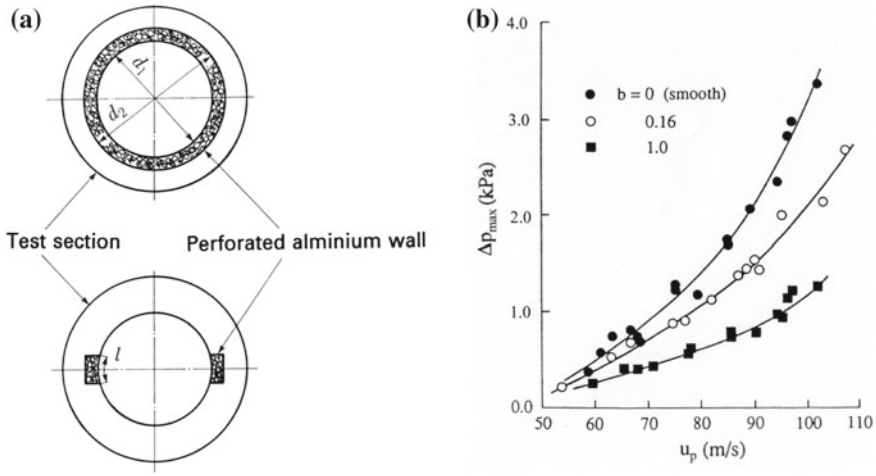


**Fig. 6.5** The effect of wall perforation on the mitigation created by the piston motion: **a** the arrangement of wall roughness; **b** the effect of the wall perforation on the shock wave attenuation

b = 1.0. The wall perforation effectively mitigates the train tunnel sonic booms and this trend is enhanced with increasing the entry speed. At $u_p$ = 70 m/s, the peak pressure along a partially roughened test section of b = 0.16 is about 15% of that along the smooth test section or b = 0, whereas the peak pressure along a totally roughened test section or b = 1.0 is reduced nearly 50% of that measured along the test section with a smooth wall.

Figure 6.6a, b show pressure histories along the roughened test section of b = 1.0 measured by distributed pressure transducers at the entry piston speeds of 98 and 65 m/s, respectively. The ordinate denotes the pressure variation on 5 kPa scale measured at the pressure transducers distributed at every 0.2 m from the entrance. The abscissa denotes the elapsed time on 10 ms scale. The pressure variation at x′ = 0.67 m shows the initial pressure variation along a smooth test section of b = 0. The initial steep pressure rise was smeared out with propagation because expansion wavelets induced from the roughened surface caught up the wave front gradually reducing its steepness. The negative pressure observed at the tail of the piston was gradually recovered as the expansion wave generated at the entry of the test section caught up the negative pressure. A similar trend is observed even at the slower entry speed of 65 m/s as seen in Fig. 6.6b. It is then concluded that roughened walls effectively attenuate the booms.

A 30 mm × 40 mm shock tube test section was connected to the 40 mm diameter smooth test section and the resulting weak shock waves running along the rectangular test section were visualized. Figure 6.7a, b show weak shock waves generated at the entry speeds of 75 and 60 m/s, respectively. The shock waves propagated from right to left. The peak over-pressures induced by these piston speeds were about 1.3 and 0.5 kPa and hence the corresponding shock Mach numbers were 1.06 and 1.02, respectively. Although a double path holographic interferometry was applied, the contrasts of these shock fronts seen in Fig. 6.7a, b are very faint because the path length of the *OB* path length was only 60 mm.

To examine the effect of wall roughness on train tunnel sonic boom's mitigation in real train's passing through a tunnel, aluminum panels each containing a 500 mm wide, 1000 mm long, and 50 mm thick aluminum foam, Alporous™, were arranged

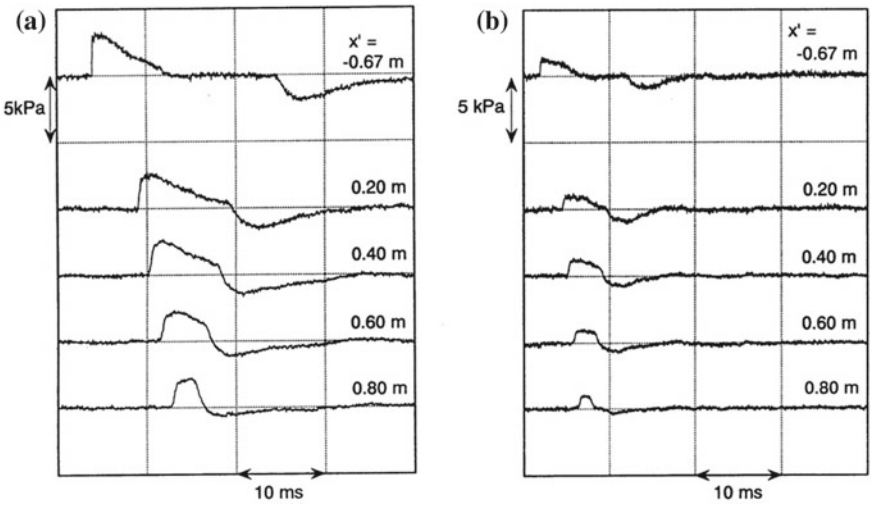


**Fig. 6.6** Formation and attenuation of a shock wave driven by a flat head piston along a perforated test section: **a** piston speed 98 m/s or 353 km/h; **b** piston speed of 65 m/s or 234 km/h

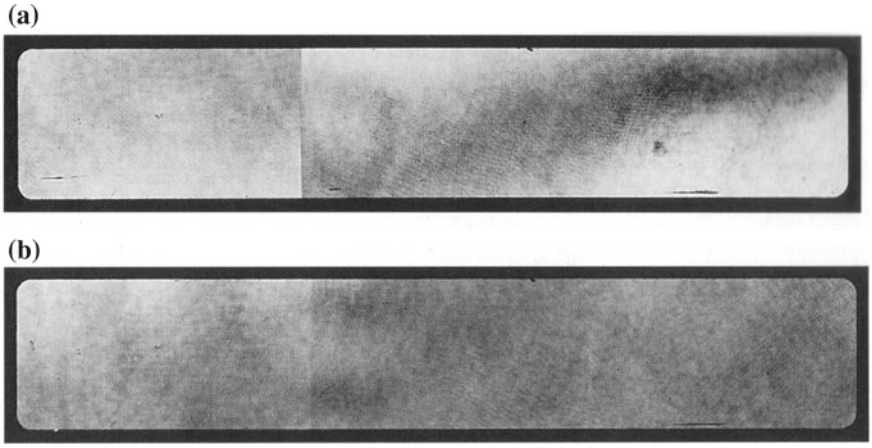


**Fig. 6.7** Weak shock waves observed in a 30 mm × 40 mm test section: **a** #93051607 piston speed of 75 m/s; **b** piston speed of 60 m/s

along the western wall starting at the 50 m distance from the north entrance of the Ichinoseki Tunnel as seen in Fig. 6.8. The booms created by the north bound trains were measured using a 100 mm diameter PVDF pressure transducer. The pressure transducer was composed of piezo film, polyvinylidene difluoride, designed and manufactured in house and calibrated in the 60 mm × 150 mm diaphragm-less shock tube by the comparison of their output signals with those obtained by Kistler pressure transducer Model 603B (Sasoh et al. 1998).

Figure 6.9a, b show the time variation of the overpressures of real train tunnel sonic booms in the absence of the porous aluminum panels and at the train speed of 245 km/s or 68 m/s. Figure 6.8b shows the time variation of the overpressure of real train tunnel sonic booms in the presence of porous aluminum panels at the train speed of 240 km/h or 64 m/s are compared. The ordinate denotes over-pressures in kPa and the abscissa denotes the elapsed time in ms. Figure 6.9a shows a steep pressure rise which implies that the boom is not mitigated. The pressure transducer had about 40 mm thick disk shape so that the high pressure behind the reflected shock wave was diffracted at the edge of the disk shaped transducer. Then the expansion wave got focused at the center and a significant pressure decrease was recorded.

Figure 6.9b shows the presence of arrayed porous aluminum plates. The peak pressure was significantly smeared out. The measured peak pressure seen in Fig. 6.9a is higher than the signal seen in Fig. 6.9b. In conclusion, the introduction of porous walls, even if it is done partially, indeed mitigated the tunnel sonic boom. The installation of aluminum foam panels on the tunnel walls effectively mitigated the booms but the price of aluminum foam panels is not inexpensive and hence it will not necessarily be economical using it in all the long High Speed Train Tunnels.

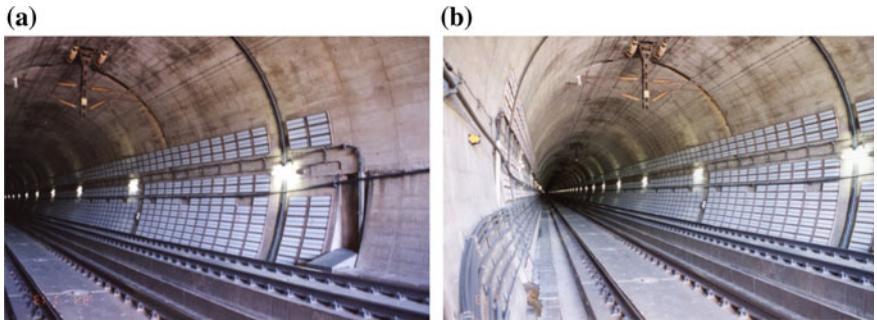


**Fig. 6.8** Framed aluminum foam panels along the western side of the Ichinoseki tunnel viewed from the north entry

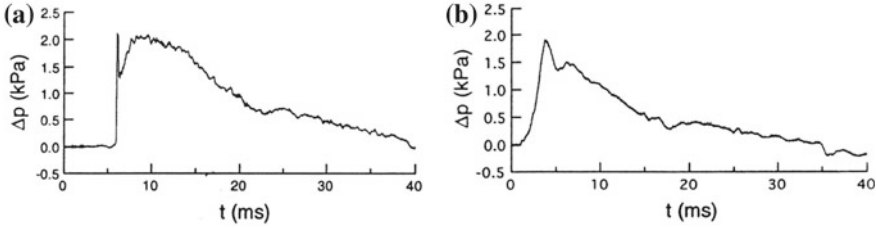


**Fig. 6.9** Pressure history of booms monitored at the Ichinoseki Tunnel: **a** absence of aluminum foam wall at train speed of 245 km/h; **b** presence of aluminum foam wall at train speed of 240 km/h (Sasoh et al. 1998)

## 6.4 Shock Wave Mitigation Along Perforated Walls

The motivation for investigating shock wave interaction with perforated walls is due to the fact that this is the simplest ways for mitigating shock wave propagating inside ducts.

### *6.4.1 Shock Wave Mitigation Along Distributed I-Beams*

Commercial aluminum I-beams of 30 mm × 100 mm and 5 mm in thickness were arranged at various combinations of heights (h) and intervals (d) inside the test section of the 60 mm × 150 mm diaphragm-less shock tube (Matsu'oka 1997). Figure 6.10a, b show the interactions of weak shock waves for Ms = 1.05 and 1.12 with 100 mm wide I-beams, 100 mm high and set at 60 mm separation. In such a long separation distance, the shock wave interacted almost independently with a single I-beam segment. The interaction with a neighboring segment is negligibly small. Figure 6.10c, d show the interaction of shock waves of Ms = 1.13 with

arrayed 100 mm wide I-beams separated at 2 mm interval. This wall shape is similar to a wall having distributed 2 mm wide slits. In comparing such a narrow separation with Fig. 6.10b, a significant deviation of the transmitted shock wave patterns was observed.

Figure 6.11 show parametric visualizations of transmitted shock waves over arrayed I-beams of various combinations of h and d. Figure 6.11a–c show shock wave interaction with arrayed I-beams of h = 8 mm and d = 4 mm for Ms = 1.02. Figure 6.11d shows the interaction for Ms = 1.12.

Figure 6.12 show shock wave mitigation along arrayed I beams of h = 8 mm and d = 7 mm for Ms = 1.12 in atmospheric air at 292 K. At each interaction with the I-beam segment, the wavelets are accumulated behind the transmitted shock wave enhancing the mitigation.

### 6.4.2 40 mm Wide Opening with Roughened Surface

In Fig. 6.13, shock wave propagations along a 40 mm wide channel with distributed shallow slits are sequentially visualized for Ms = 1.22 in atmospheric air at 294 K. The test model was installed in the 60 mm × 150 mm diaphragm-less shock tube. At first the IS was diffracted at the entrance corners and then the resulting transmitted shock wave interacted with each slit showing complex wave interaction patterns and promoted mitigation. The test piece was installed in the 60 mm × 150 mm diaphragm-less shock tube. Figure 6.13c shows an enlargement of Fig. 6.13b: an earlier stage of shock wave propagation along the distributed slits. Expansion waves were generated from the slit openings and compression waves are generated from the bottom of the slits. These wavelets interacted with the transmitted shock wave and attenuated the transmitted shock wave. In Fig. 6.13e, f, the transmitted shock wave is seen from the exit and was diffracting at the exit corners. The evolution of the resulting pair vortices indicates that the attenuation of the shock wave is attenuated upon it a release from the exit.

### 6.4.3 25 mm Wide Opening with Smooth Surface

In Fig. 6.14, the evolution of shock wave along a 25 mm wide duct with smooth wall was visualized for Ms = 1.20 in atmospheric air at 296.8 K. Comparing to the case of shock wave interaction with a wall having distributed slits, as shown in Fig. 6.13, the transmitted shock wave was not strongly disturbed while progressing along the smooth wall. The fringes were uniformly distributed in this case. The shear flows in the boundary layer are released from the exit forming a series of vortices as seen in Fig. 6.14f, g.

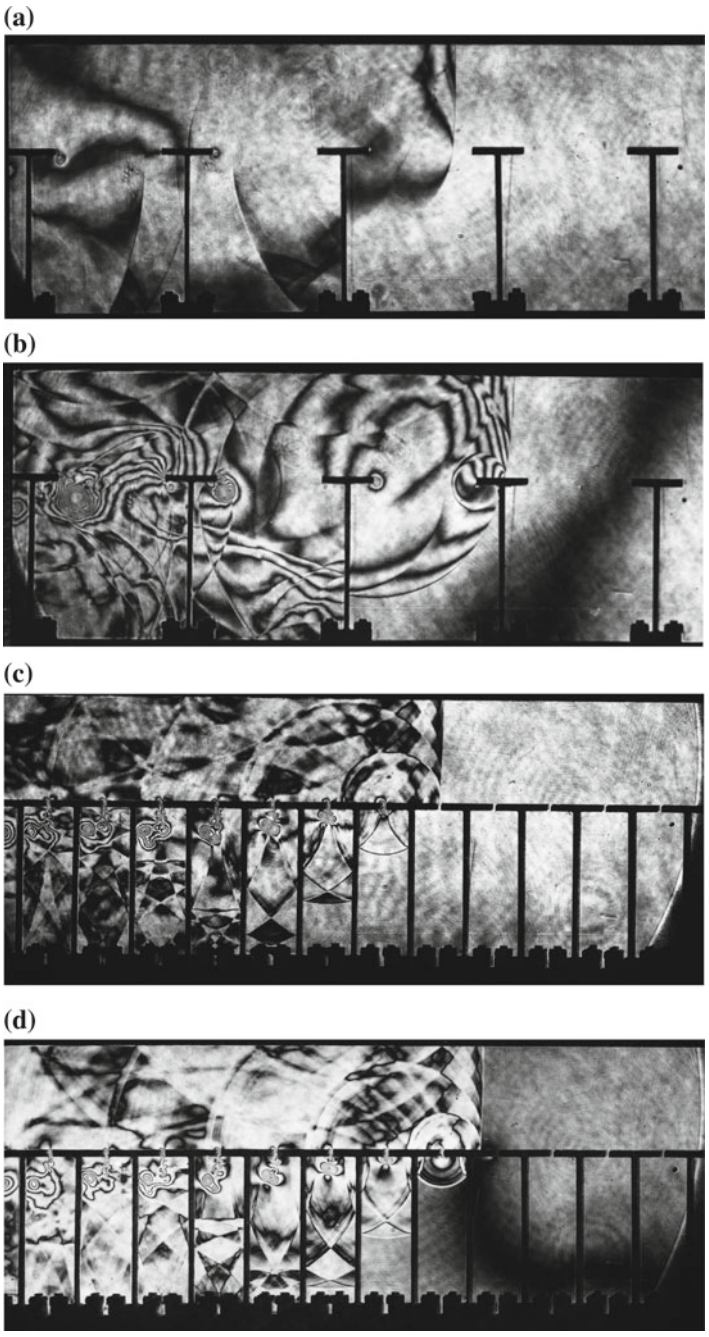


**Fig. 6.10** Shock wave mitigation along a perforated wall of h = 100.0 mm in atmospheric air at 292 K: **a** #96050210, Ms = 1.048, d = 60 mm; **b** #96050204, Ms = 1.123, d = 60 mm; **c** #96043002, Ms = 1.13, d = 2 mm; **d** #96042542, Ms = 1.13, d = 2 mm (Matsuoka 1997)

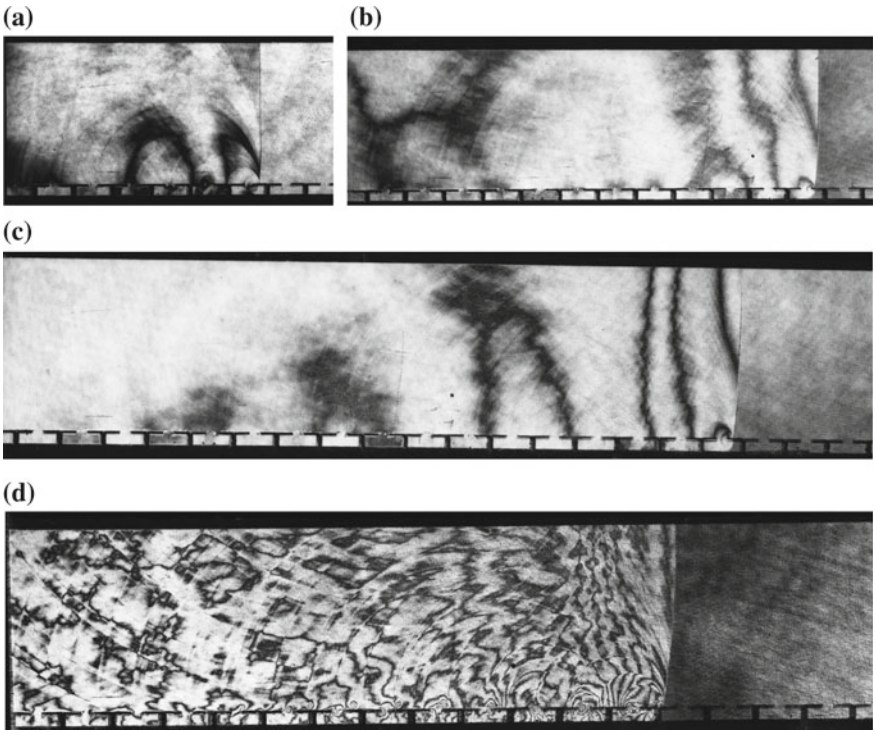


**Fig. 6.11** Shock wave mitigation along arrayed I beams of h = 8 mm and d = 4 mm for Ms = 1.02 in atmospheric air at 292 K: **a** #96061708; **b** #96061705; **c** #96061707; and **d** #96061910 for Ms = 1.12

### *6.4.4 10 mm Wide Opening with Smooth Surface*

Figure 6.15 show the evolution of shock wave propagation along a 10 mm wide opening for Ms = 2.7 in air at 100 hPa, 285.8 K. The transmitted shock wave created by diffraction at the entrance corner generated wavelets as seen in Fig. 6.15a, b. The fringe observed parallel to the wall exhibited shows the boundary layer developing along the smooth wall. It develops independently of the width of the opening. In the present experiments with smooth wall model it is the boundary layer that governs the shock wav attenuation. Hence the smaller the opening width is, the more effectively the shock wave would be attenuated.

Shock wave propagation along a 6.0 mm wide opening was sequentially observed. This arrangement was used to produce a narrow shock wave which was needed to interact with a 6 mm high circular soap column. For producing undisturbed shock tube flows propagating in a narrow shock tube, a so-called cookie cutter was used. The cookie cutter was installed in the 60 mm × 150 mm diaphragm-less shock tube.

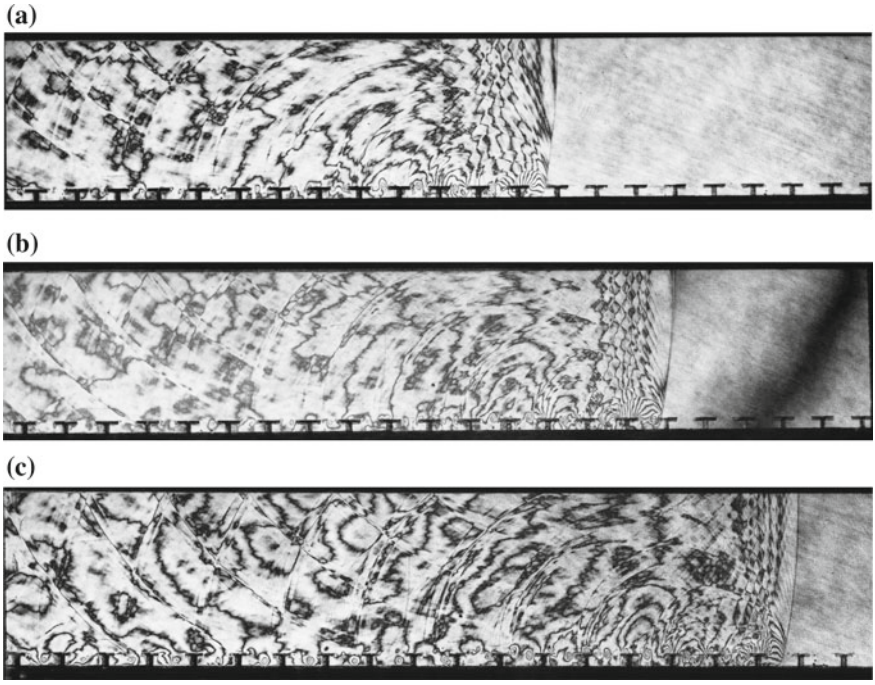


**Fig. 6.12** Shock wave mitigation along arrayed truncated I-beams of h = 8 mm and d = 7 mm for Ms = 1.12 in atmospheric air at 292 K: **a** #96061906; **b** #96061201; **c** #96061205

Figure 6.16 show the evolution of shock wave propagating along a 6 mm wide opening for Ms = 1.4 in air at 100 hPa, 285.8 K. In Fig. 6.16a, b, as the leading edge has a sharp edge, the shock wave diffraction at the entrance is hardly seen. Hence, the transmitted shock wave is undisturbed and the flow behind it is uniform. This test section would be an effective cookie cutter, if a 6 mm wide test section is positioned at an appropriate distance from the leading edge.

## 6.5 Shock Wave Mitigation Passing Through a Small Hole

### *6.5.1 A Single Hole*

Figure 6.17 show the evolution of the shock wave propagating through a 5 mm diameter hole drilled on a 30 mm thick wall for Ms = 1.27 in atmospheric air at 292 K. A 30 mm thick stainless steel wall was installed in the 60 mm × 150 mm diaphragm-less shock tube. The incident shock wave, IS, reflected from the steel plate but part of the IS propagated through the thin hole and a transmitted shock wave came from the hole.

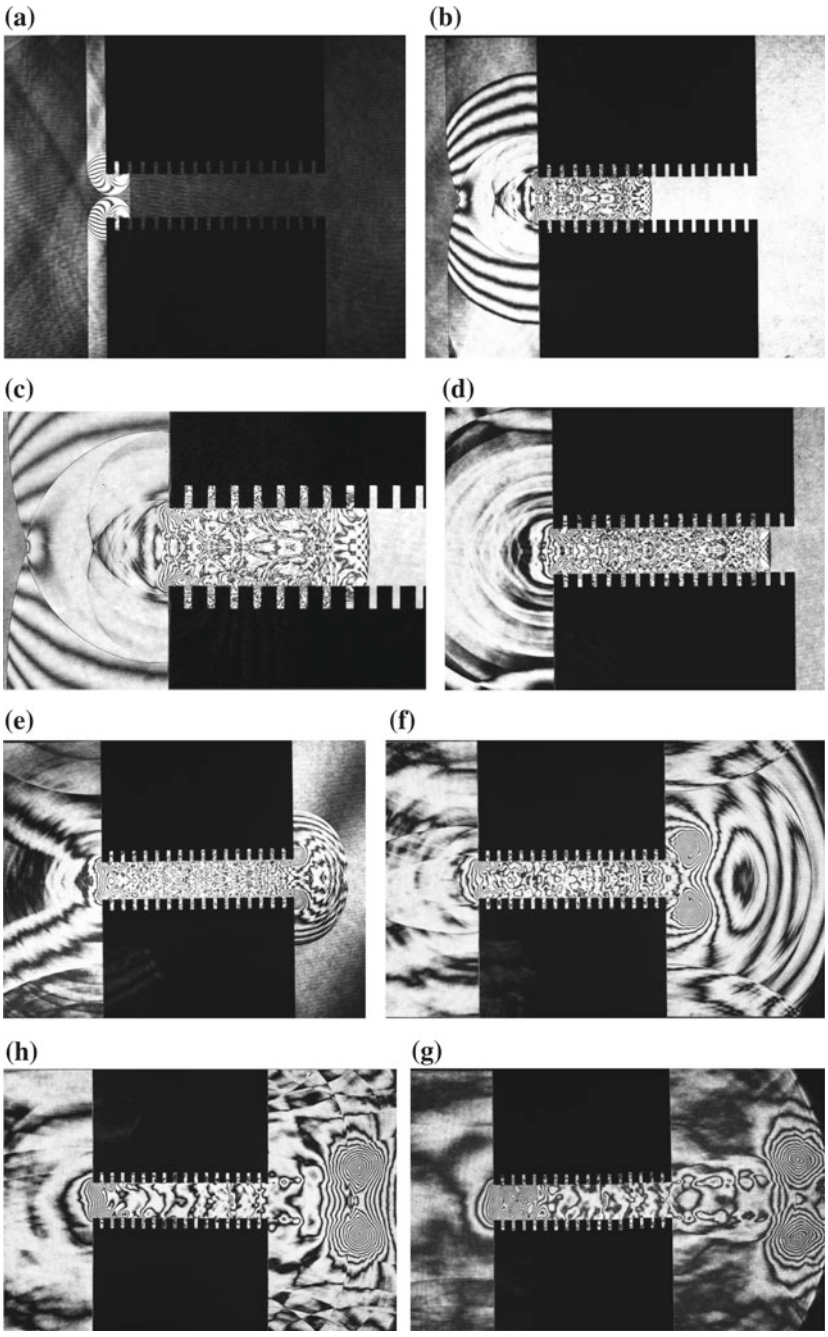


**Fig. 6.13** Shock wave propagation along distributed slits for Ms = 1.22 in atmospheric air at 294 K: **a** #9304270; **b** #93042702, 500 μs from trigger point, Ms = 1.223; **c** enlargement of (**b**; **d** #93042703, 600 μs, Ms = 1.223; **e** #93042704, 700 μs, Ms = 1.218; **f** #93042705, 900 μs, Ms = 1.215; **g** #93042706, 1300 μs, Ms = 1.212; **h** #93042707, 1500 μs, Ms = 1.215

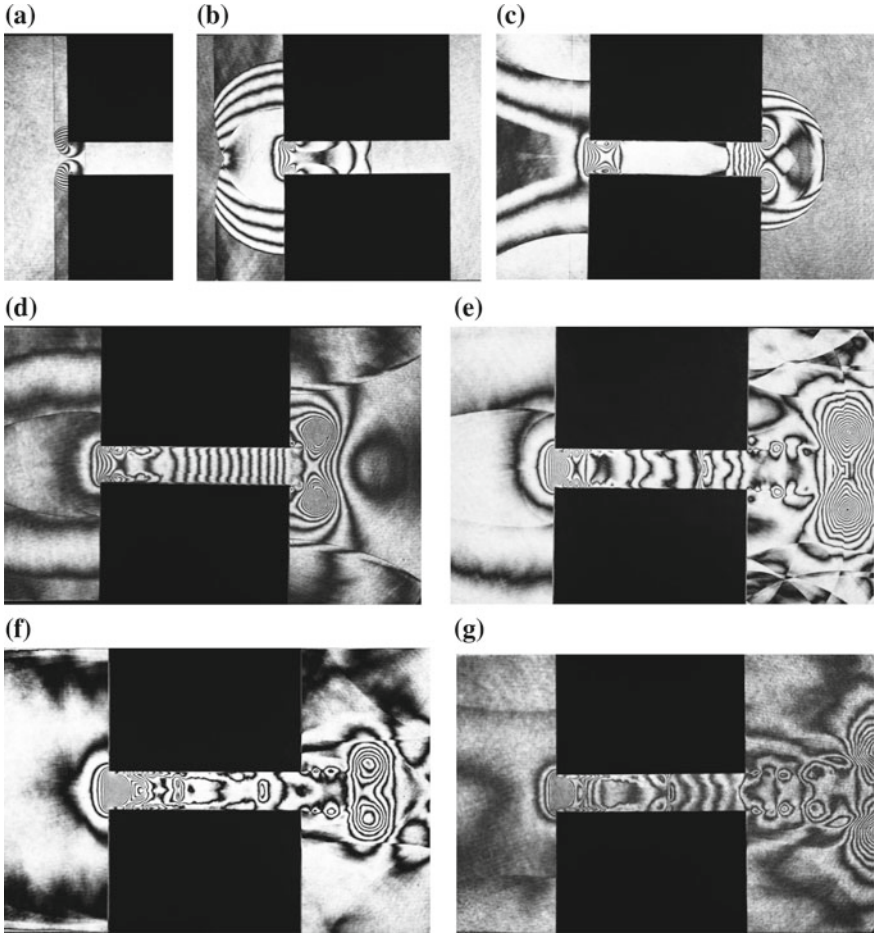


**Fig. 6.14** The evolution of shock wave mitigation along a slotted wall with smooth surface for Ms = 1.20 in atmospheric air at 296.8 K: **a** #93042618, 100 μs from trigger point, Ms = 1.208; **b** #93042617, 300 μs, Ms = 1.212; **c** #93042615, 500 μs, Ms = 1.208; **d** #93042614, 900 μs, Ms = 1.208; **e** #93042613, 1300 μs, Ms = 1.208; **f** #93042612, 1300 μs, Ms = 1.267; **g** #93042611, 1500 μs, Ms = 1.219

### *6.5.2 Two Oblique Holes*

Figure 6.18 show the evolution of shock wave mitigation through two 5 mm diameter obliquely drilled holes for Ms = 2.26 in air at 250 hPa, 290 K. The two holes were separated by 10 mm interval were drilled obliquely 30° on s 30 mm thick stainless steel plate. The plate was installed in the in the 60 mm × 150 mm diaphragm-less shock tube. This was a part of basic experiment related to the study of the suppression of automobile exhaust gas noise. The sequence of the merger of the two transmitted shock waves into a single shock wave was visualized.

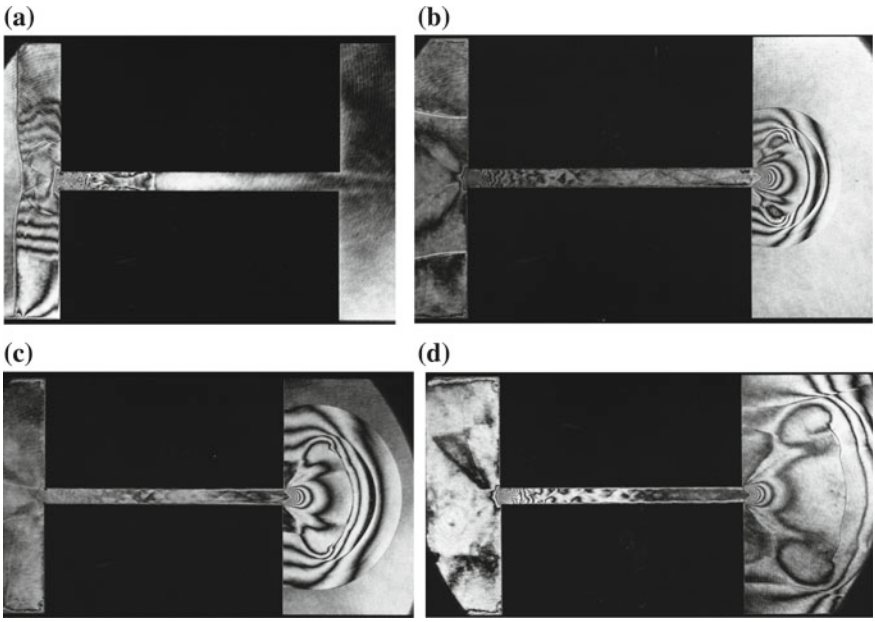


**Fig. 6.15** Evolution of shock wave propagation along a 10 mm wide opening for Ms = 2.7 in air at 100 hPa, 285.8 K: **a** #85041502, 70 μs from trigger point, Ms = 2.215; **b** #85041504, 90 μs, Ms = 2.702; **c** #85041507, 130 μs, Ms = 2.711; **d** #85041508, 200 μs, Ms = 2.741

Figure 6.18a shows two spherical shock waves released from the oblique holes. Figure 6.18d–f show the process of two spherical shock waves gradually merging into a single shock wave.

Two 5 mm diameter holes were drilled obliquely at 7.5 mm interval vertical to the center line of a 30 mm thick stainless steel plate. The two holes merged at the center of the plate. Figure 6.19a shows the obliquely drilled holes and the early stage of the shock wave transmission through the oblique holes. The shock waves entering the oblique holes merged at the exit. Figure 6.19g explains two 5 mm diameter holes obliquely drilled at 7.5 mm interval at the frontal surface merged into a hole at the rear surface.

## 6.6 Sintered Stainless Steel Walls

1 mm thick sintered stainless steel plates were placed on the upper and lower walls of the 100 mm × 200 mm test section as seen in Fig. 6.20. This test section was accommodated in the 150 mm × 250 mm test section connected to the 60 mm 150 mm conventional shock tube. The sequential observation of shock wave attenuation along two 1 mm thick sintered stainless steel plates was conducted for Ms = 1.06 in atmospheric air at 290.8 K.

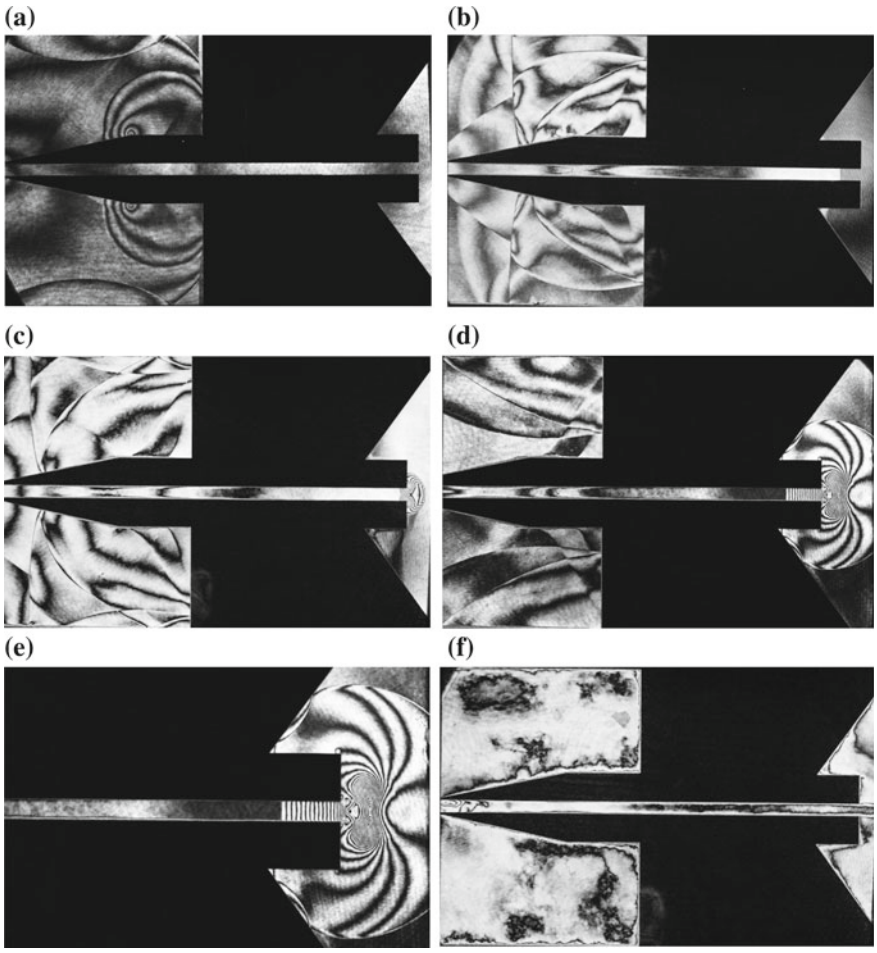


**Fig. 6.16** The evolution of shock wave propagating along a 6 mm wide opening for Ms = 1.4 in air at 100 hPa, 285.8 K: **a** #86120204, 330 μs, Ms = 1.402; **b** #86120308, 440 μs, Ms = 1.420; **c** #86120301, 460 μs, Ms = 1.420; **d** #86120305, 480 μs, Ms = 1.420; **e** enlargement of (**d**); **f** #86120303, 500 μs, Ms = 1.408

The sintered stainless steel plates had many minute perforations evenly distributed on its surface but the surface was so smooth that it was an ideal material for attenuating weak shock waves like those seen induced in the automobile exhaust gas pipe line systems. The sintered stainless steel plates were strong enough to withstand against relatively high pressure loading. Although its physical properties were wonderful but his material was not easy to be used in applications like the one considered. In the series of experiments, the space behind the sintered stainless steel was open and then the transmitted shock waves were just reflected from the test section wall. For efficiently attenuating the transmitted shock wave, appropriate materials should be inserted behind the sintered stainless plates.

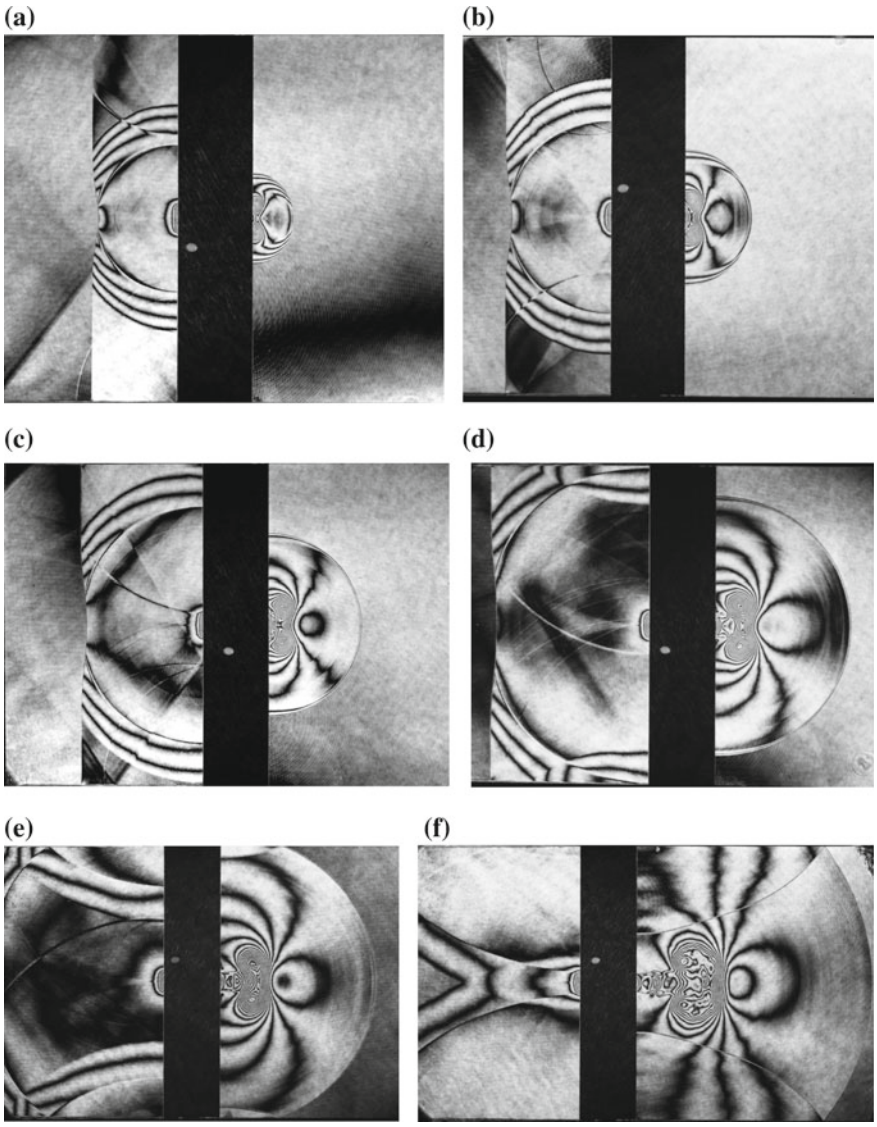


**Fig. 6.17** The evolution of the shock wave propagating through a 5 mm diameter hole on a 30 mm thick wall for Ms = 1.27 in atmospheric air at 292 K: **a** #91111428, 330 μs; **b** #91111423, 360 μs; **c** #91111424, 400 μs; **d** #91111425, 450 μs; **e** #91111426, 510 μs; **f** #91111427, 620 μs

Figure 6.21 show the shock wave mitigation along the sintered stainless plates backed up with solid walls for moderate shock wave of Ms = 1.38 in air at 600 hPa, 290.8 K.

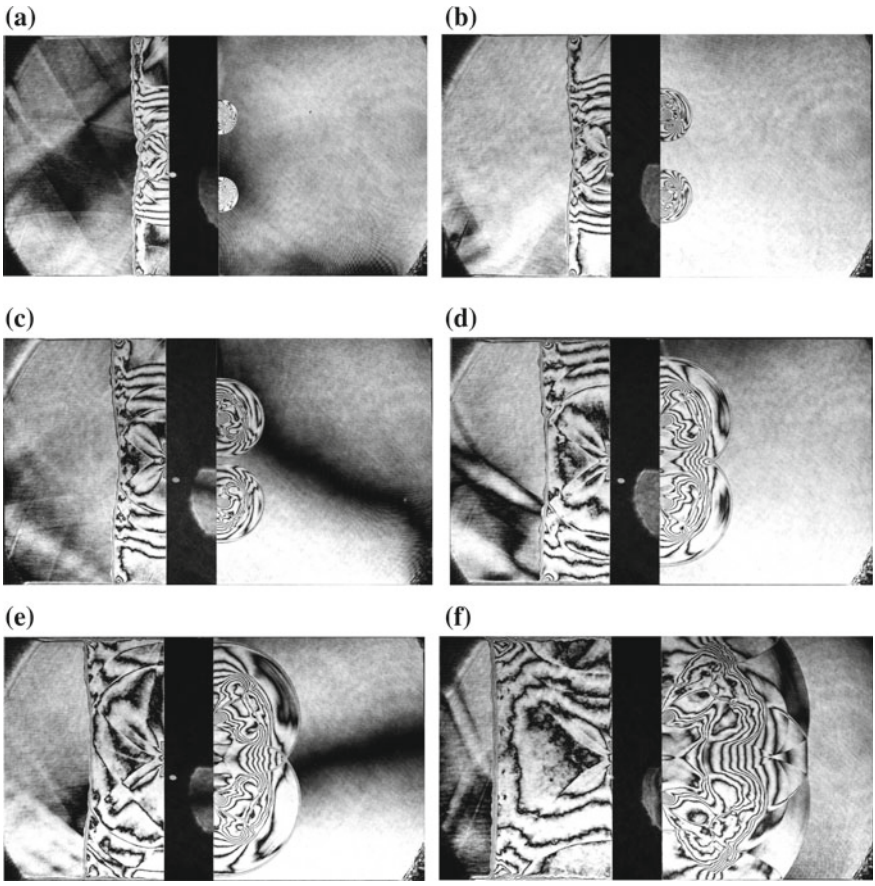


**Fig. 6.18** Shock wave mitigation through two holes for Ms = 2.26 in air at 250 hPa, 290 K, two 5 mm diameter holes separated by 10 mm diverging 30°: **a** #91111819, 270 μs from trigger point, Ms = 2.185; **b** 91111820, 280 μs; **c** #91111821, 300 μs; **d** #91111822, 330 μs; **e** #91111823, 370 μs; **f** #91111824, 420 μs

### *6.6.1 Sintered Stainless Wall Backed up with Alporous$^{TR}$*

In this sonic boom experiments, aluminum sponge, the trade name Alporous$^{TR}$, was frequently used. Figure 6.22 show a sequence of shock wave attenuation along the sintered stainless steel plates backed up with Alporous$^{TR}$.

### *6.6.2 Perforated Walls*

Figure 6.23 show a sequential observation of shock wave propagation along a perforated wall. The perforated wall shown in Fig. 2.23 had 1.0 mm diameter holes

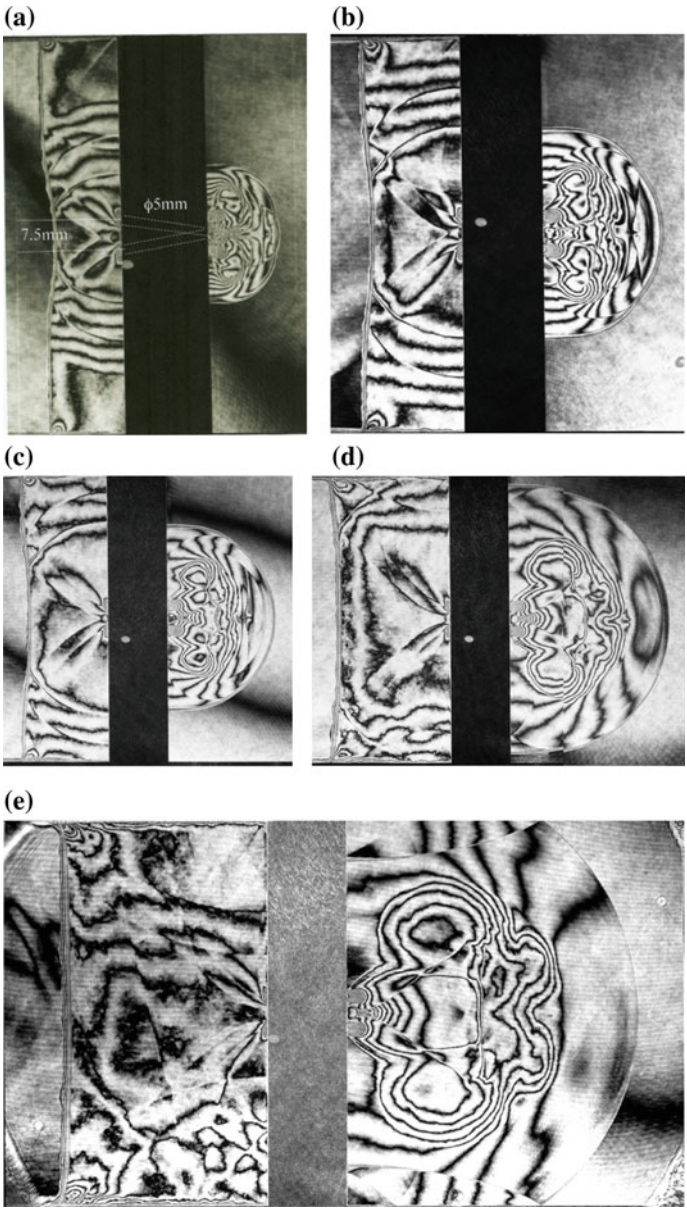


**Fig. 6.19** The evolution of the shock wave attenuation through two 5 mm diameter holes separated in 7.5 mm interval for Ms = 2.20 in air at 250 hPa, 290.5 K: **a** #91111514, 280 μs, Ms = 2.188; **b** #91111515, 300 μs, Ms = 2.235; **c** #91111516, 330 μs, Ms = 2.188; **d** #91111517, 370 μs, Ms = 2.239; **e** #91111518, 420 μs, Ms = 2.239

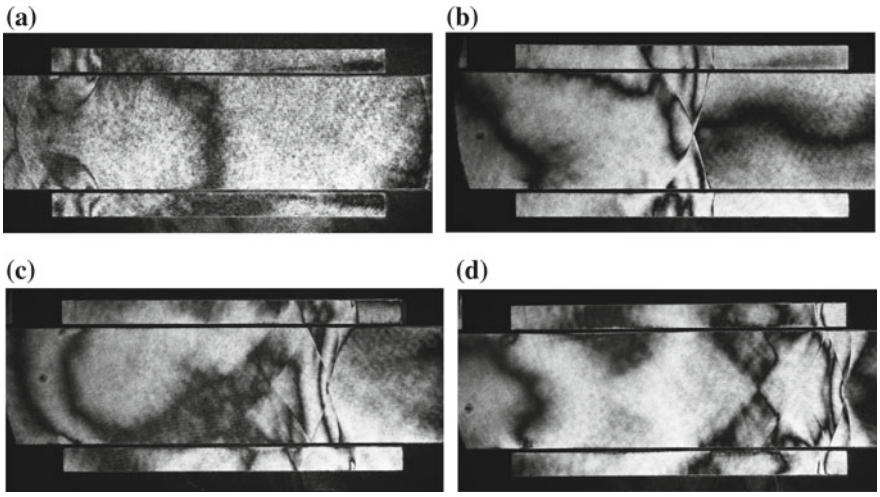


**Fig. 6.20** Shock wave mitigation along sintered stainless plates backed up with solid walls for Ms = 1.06 in atmospheric air at 290.8 K: **a** #92011702, 800 μs, Ms = 1.069; **b** #92011703, 950 μs, Ms = 1.067; **c** #92011705, 1250 μs, Ms = 1.067; **d** #92011706, 1400 μs, Ms = 1.080

were uniformly distributed on a 2.0 mm thick brass plates; the perforation ratio was 0.5. The opening width was 30 mm and the supporting side wall was 40 mm wide.

Figure 6.24 show the evolution of shock wave attenuation along the perforated wall having perforation ratio of 0.2 for Ms = 2.50 in air at 333 hPa, 290 K. The inclination angle θ of the transmitted shock wave propagating along the upper and lower walls indicates approximately $\sin\theta = a/u_s$ where a is the sound speed in air and $u_s$ is the speed of the transmitted shock wave. Therefore, measuring the θ, the transmitted shock wave attenuation is readily estimated.

### *6.6.3 Wall with Slotted Surfaces*

The transition of the reflected shock waves from the slotted wedge was discussed in the Chap. 2 and the slot geometry of the slotted was described in Fig. 2.44. Figure 6.25a shows the slotted wall: the wall was 100 mm long and the slots were 7 mm deep: it was tested in the 60 mm × 150 mm conventional shock tube.

The shock wave propagation along a tested slotted wall placed at the bottom of the test section of the shock tube were sequentially visualized for Ms = 1.40 in atmospheric air at 293.7 K. Figure 6.25 show sequential observation of shock wave propagating along the slotted wall. The shock wave interacted with individual slots creating the wavelets that successively promoted mitigation. Figure 6.25 explains these generation of wavelets (Onodera and Takayama 1990).

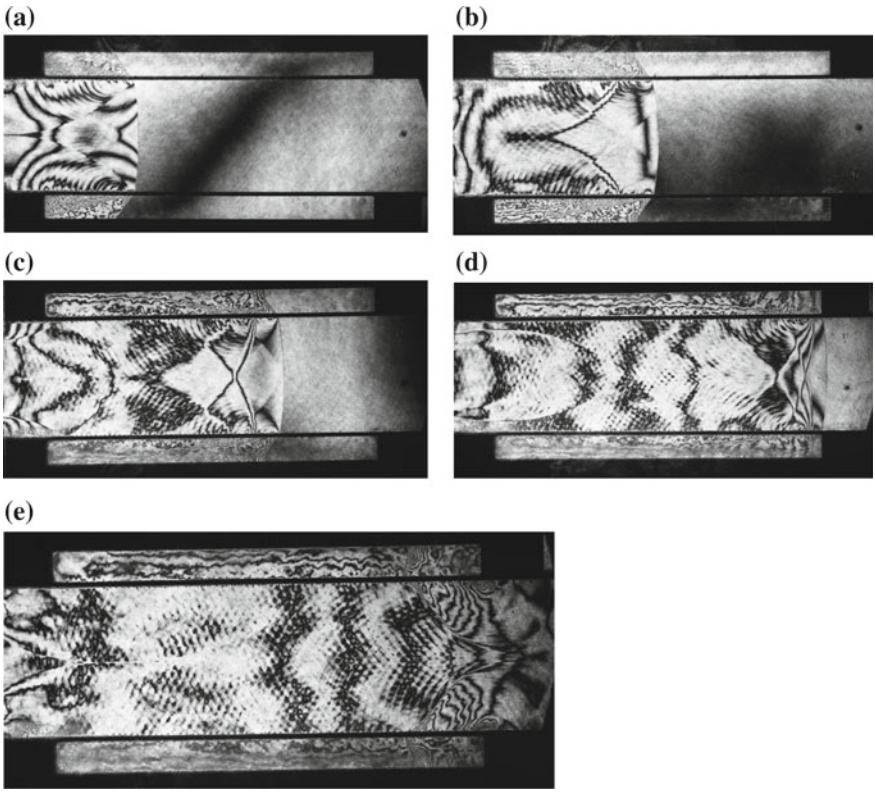


**Fig. 6.21** Shock wave mitigation along the sintered stainless plates backed up with solid walls for Ms = 1.38 in air at 600 hPa, 290.8 K: **a** #92011711, 600 μs from trigger point, Ms = 1.392; **b** #92011712, 900 μs, Ms = 1.380; **c** #92011713, 800 μs, Ms = 1.390; **d** #92011714, 940 μs, Ms = 1.393; **e** #92011715, 1060 μs, Ms = 1.384

### *6.6.4 Distributed Slit Wall*

A 150 mm × 230 mm test piece having distributed slits was placed on the upper and lower walls were inserted into the 150 mm × 250 mm test section of the 60 mm × 150 mm conventional shock tube. Figure 6.26 show shock wave propagation along slit walls for Ms = 1.40 in atmospheric air at 294.3 K. Irregularly shaped grey patterns observed in Fig. 6.26a were compression waves leaked through a narrow gap between the test piece and the shock tube side walls. Such compression waves merged with the transmitting shock wave and were not observable in Fig. 6.26b.

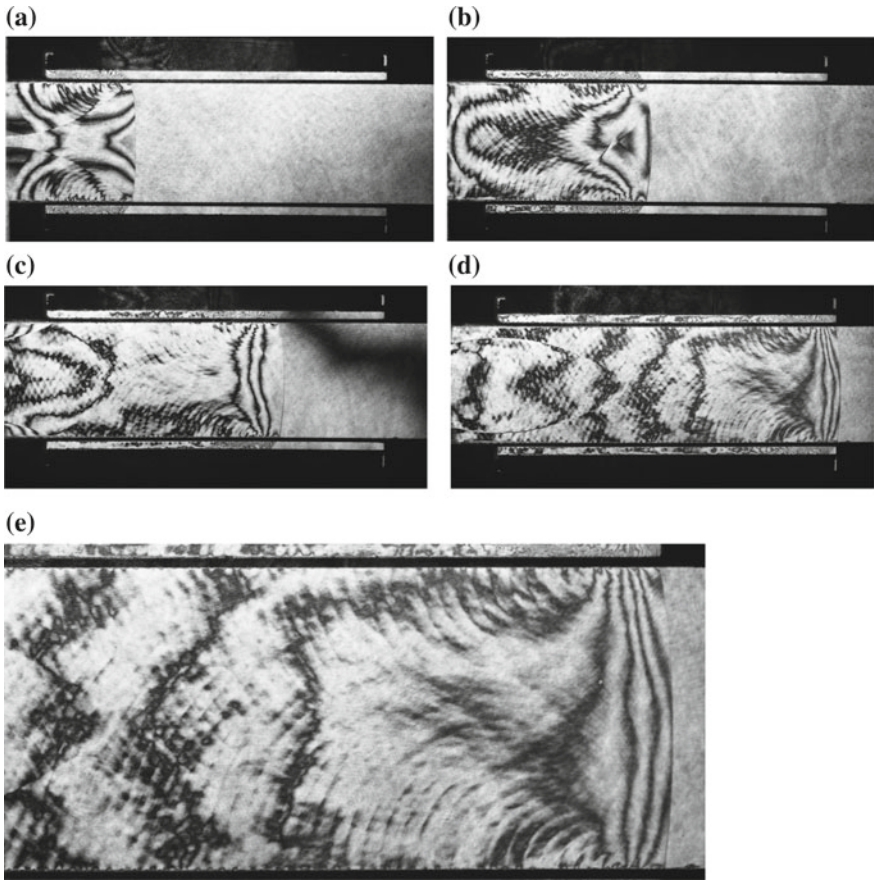


**Fig. 6.22** Evolution of shock wave propagating along sintered stainless steel plates backed up with Alporous[TR] wall for Ms = 1.40 in atmospheric air at 290.8 K: **a** #92011808, 600 μs from the trigger point, Ms = 1.399; **b** #92011809, 700 μs, Ms = 1.396; **c** #92011810, 800 μs, Ms = 1.396; **d** #92011811, 940 μs, Ms = 1.401; **e** enlargement of (**d**)

## 6.7 Alporous[TR] Walls

Figure 6.27 show the evolution of the shock wave propagation along aluminum sponge Alporous[TR] walls for Ms = 1.15 in atmospheric air at 282.0 K. The upper and lower walls and the both sides of the 150 mm × 250 mm test section were covered with a 10 mm thick Alporous[TR]. It proved to be a useful material as liners for suppressing shock waves generated along engine exhaust gas pipe lines. Covering the test section with liners of Alporous[TR] as shown in Fig. 6.27a does not eliminate the twin vortices at the test section entrance.

The shock wave was not reflected from the Alporous[TR] liners but was transmitted from the bottom of the liners. It was reconfirmed to be a good material for

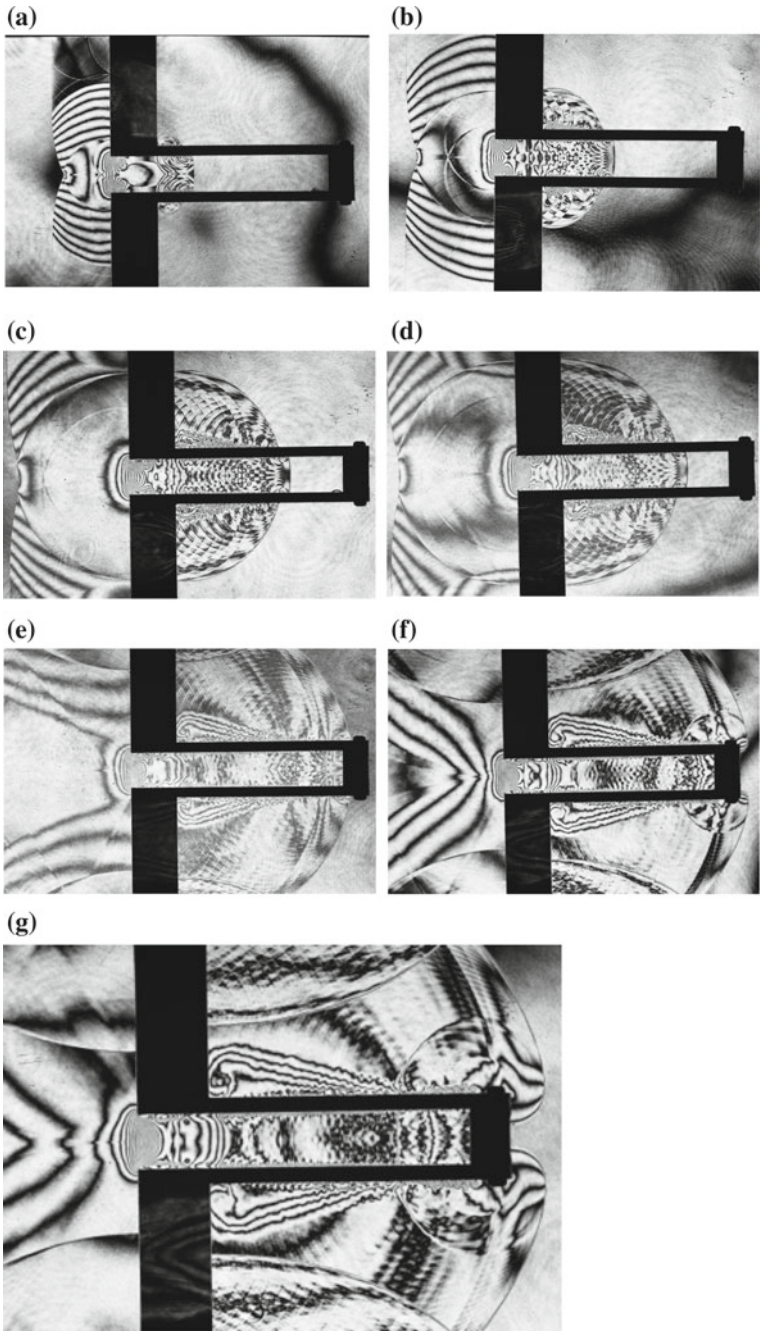


**Fig. 6.23** Shock wave propagation along the perforated wall having perforation ratio 0.5 for Ms = 1.30 in air at 900 hPa, 292.7 K: **a** #87030415, Ms = 1.302; **b** #87030409, Ms = 1.260; **c** #87030303, Ms = 1.219; **d** #87030401, Ms = 1.217; **e** #87030405, Ms = 1.259; **f** #87030407, Ms = 1.257; **g** #87030413, 700 μs, Ms = 1.254

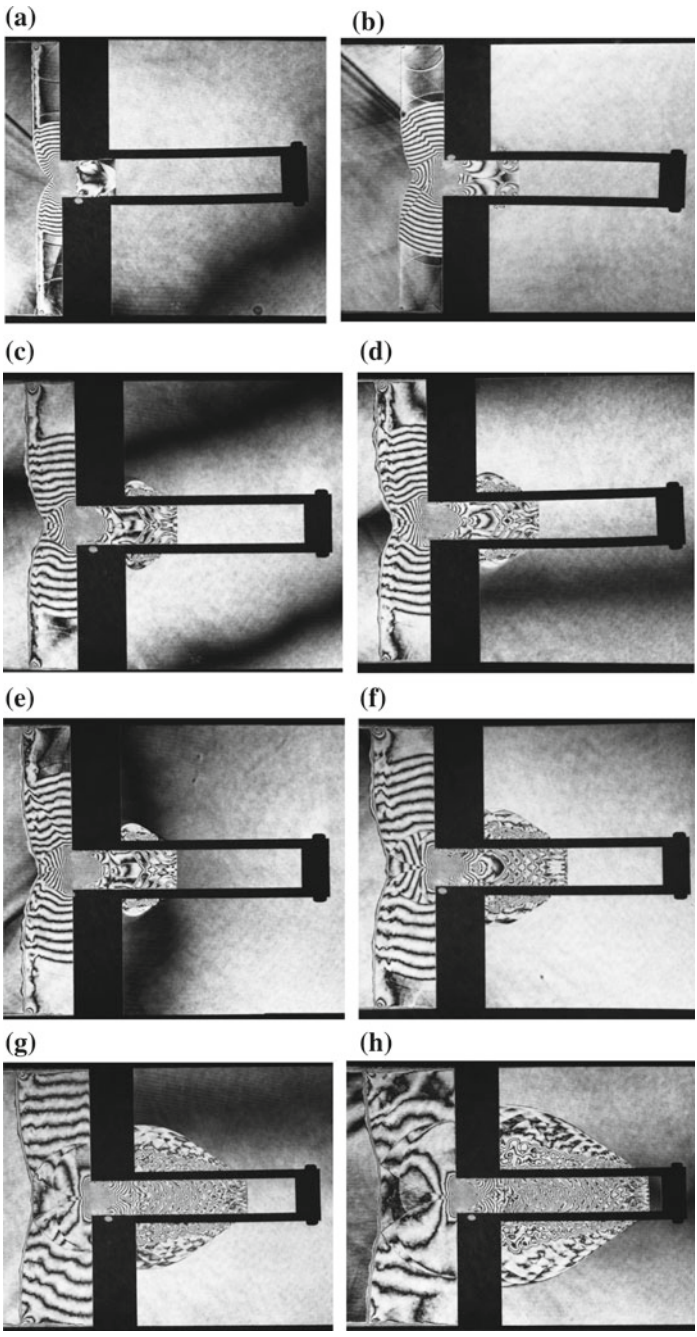


**Fig. 6.24** The evolution of the shock wave propagating along a perforated wall having perforation ratio 0.2 for Ms = 2.50 in air at 333 hPa, 290 K: **a** #91111408, Ms = 2.560; **b** #91111416, Ms = 2.429; **c** #91111402, Ms = 2.560; **d** #91111409, Ms = 2.429; **e** #91111403, Ms = 2.560; **f** #91111404, Ms = 2.307; **g** #91111405, Ms = 2.209; **h** #91111406, Ms = 2.560

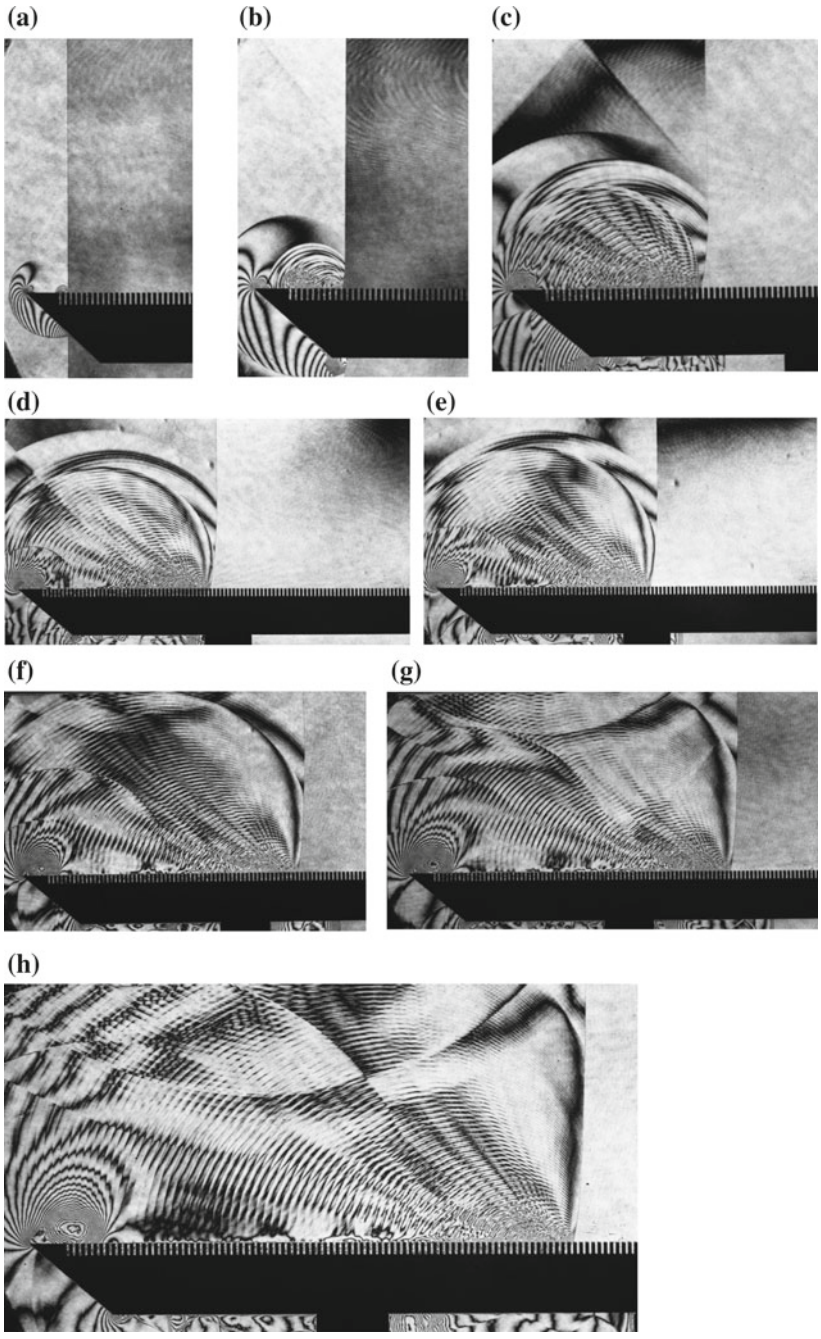


**Fig. 6.25** Shock wave propagation along a slotted wall for Ms = 1.40 in atmospheric air at 293.7 K: **a** #87052520, Ms = 1.431; **b** #87052503, Ms = 1.415; **c** #87052506, Ms = 1.431; **d** #87052509, Ms = 1.418; **e** #87052510, Ms = 1.418; **f** #87052512, Ms = 1.422; **g** #87052514, Ms = 1.426; **h** #87052516, Ms = 1.426

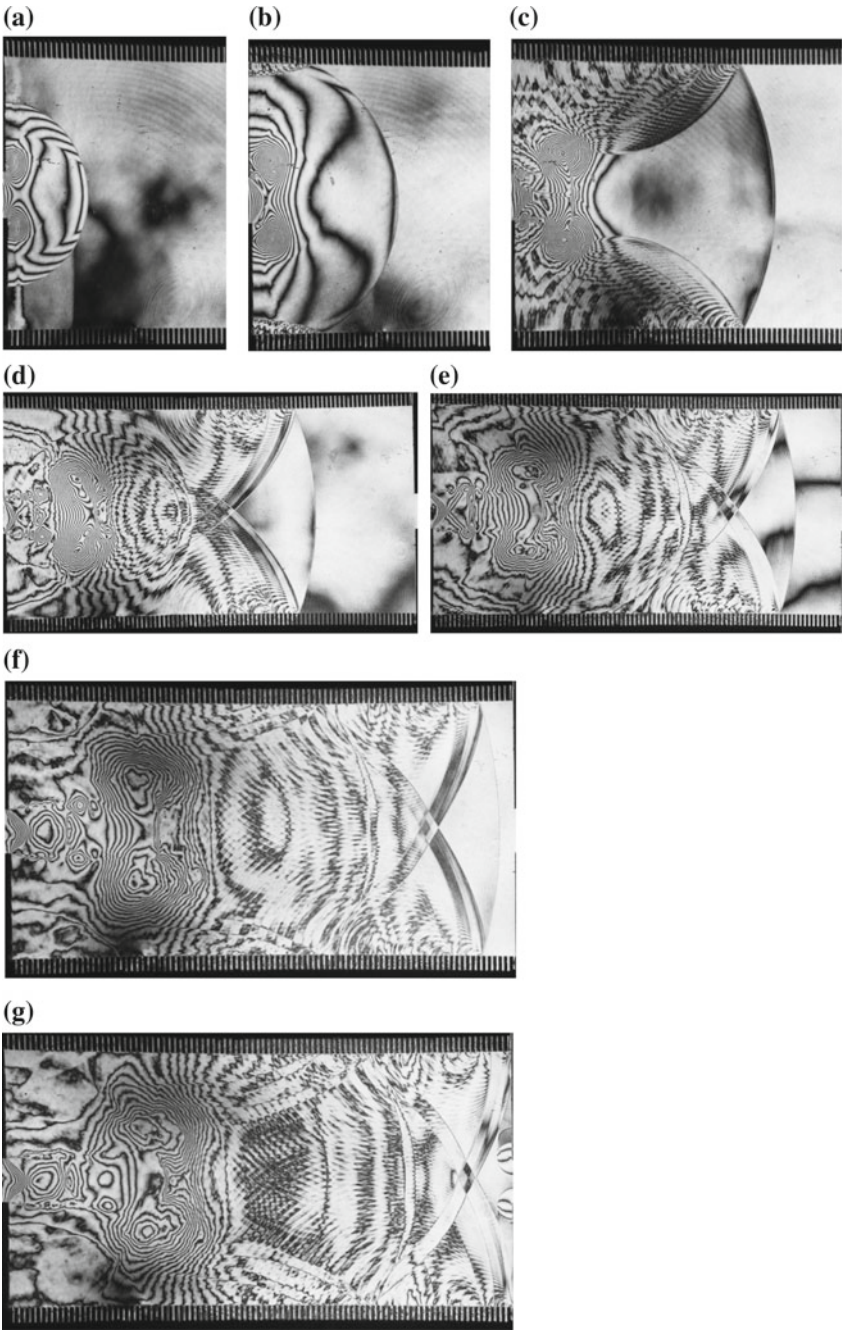


**Fig. 6.26** Shock wave propagation along slit wall for Ms = 1.40 in atmospheric air at 294.3 K: **a** #90092811; **b** #90092810; **c** #90092809; **d** #90092807; **e** #90092807; **f** #90092808

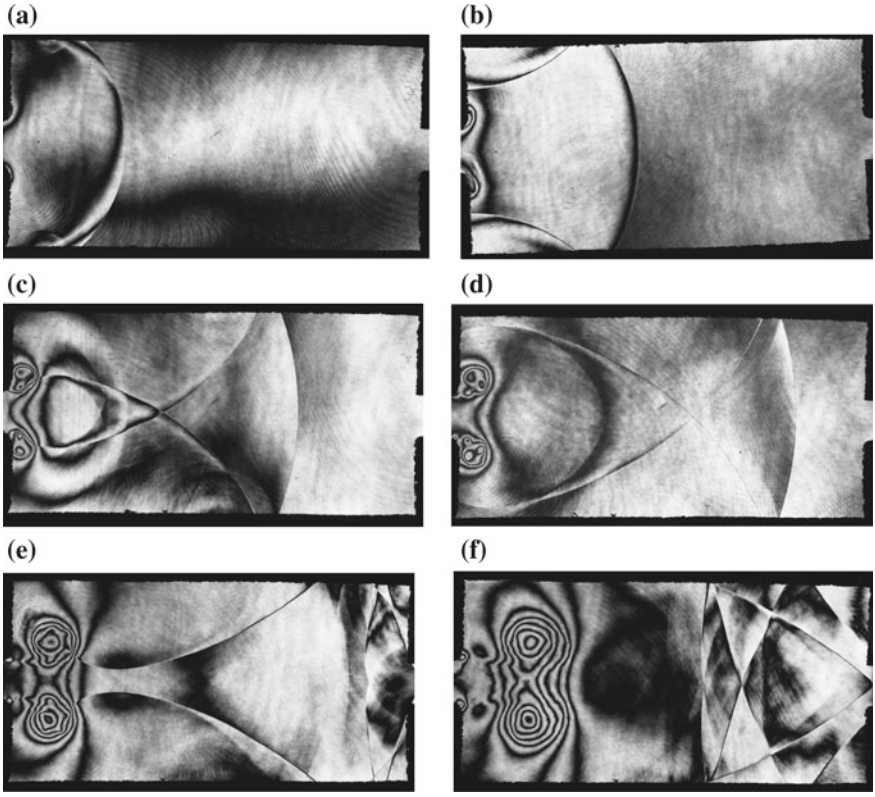


**Fig. 6.27** The evolution of the shock wave propagation along aluminum sponge (Alporous$^{TR}$) walls for Ms = 1.15 in atmospheric air at 282.0 K: **a** #88011907, 350 μs, Ms = 1.145; **b** #88011908, 430 μs, Ms = 1.153; **c** #88011910, 590 μs, Ms = 1.153; **d** #88011911, 670 μs, Ms = 1.147; **e** #88011913, 900 μs, Ms = 1.151; **f** #88011914, 1100 μs, Ms = 1.157

mitigating shock waves. Reflected shock waves became gradually faint during their propagation.

In the case of very weak shock waves shown in Fig. 6.28, the transmitted shock wave became faint. In Fig. 2.28f, no distinct reflections are observed. It should be emphasized that the Alporous$^{TR}$ is a good material for liners in silencers.

## 6.8 Shock Wave Mitigation While Passing Through Multiple Partitions

When entering into layers of partitions, the shock wave repeatedly reflected back and forth between the obstacles. Such multiple diffractions and reflections lead to promote the mitigation of shock waves. The transmitted shock waves also

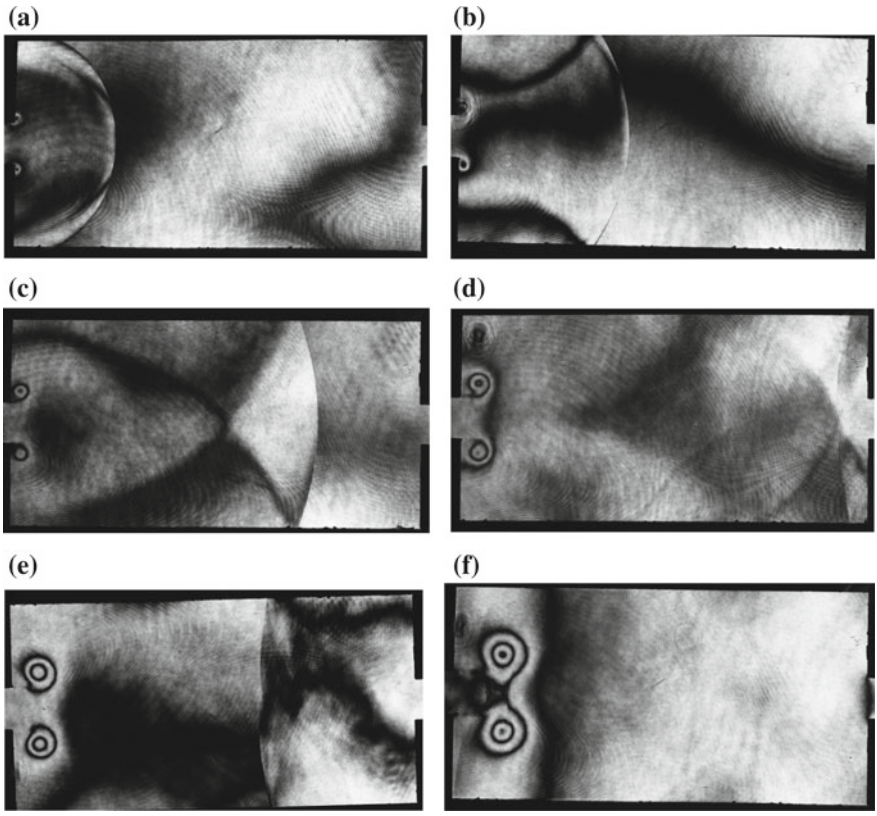


**Fig. 6.28** The revolution of shock wave propagation along the Alporous$^{TR}$ walls for Ms = 1.08 in atmospheric air at 282.0: **a** #88012005, 400 μs from trigger point, Ms = 1.082; **b** #88012007, 700 μs, Ms = 1.084; **c** #88012007, Ms = 1.084; **d** #88012008, 900 μs, Ms = 1.086; **e** #88012009, 1100 μs, Ms = 1.086; **f** #88012010, 1500 μs, Ms = 1.081

interacted with sidewalls. The entire wave interaction results in a complex flow field containing triple points accompanied with slip lines or vortices, which effectively promote the attenuation of the transmitted shock wave. The shock wave mitigation amount depends on the specific geometry of the partitions. Dependence of the shock wave mitigation on the partition geometry is discussed here. A comparison between numerical simulations and interferograms describing shock wave passing through different partitions would be an interesting bench mark test.

### *6.8.1 Mitigation Through Partitions*

Figure 6.29a–j show one of the simplest partition: a 150 mm × 250 mm test section was split into 50 mm wide partitions. The transmitted shock wave created

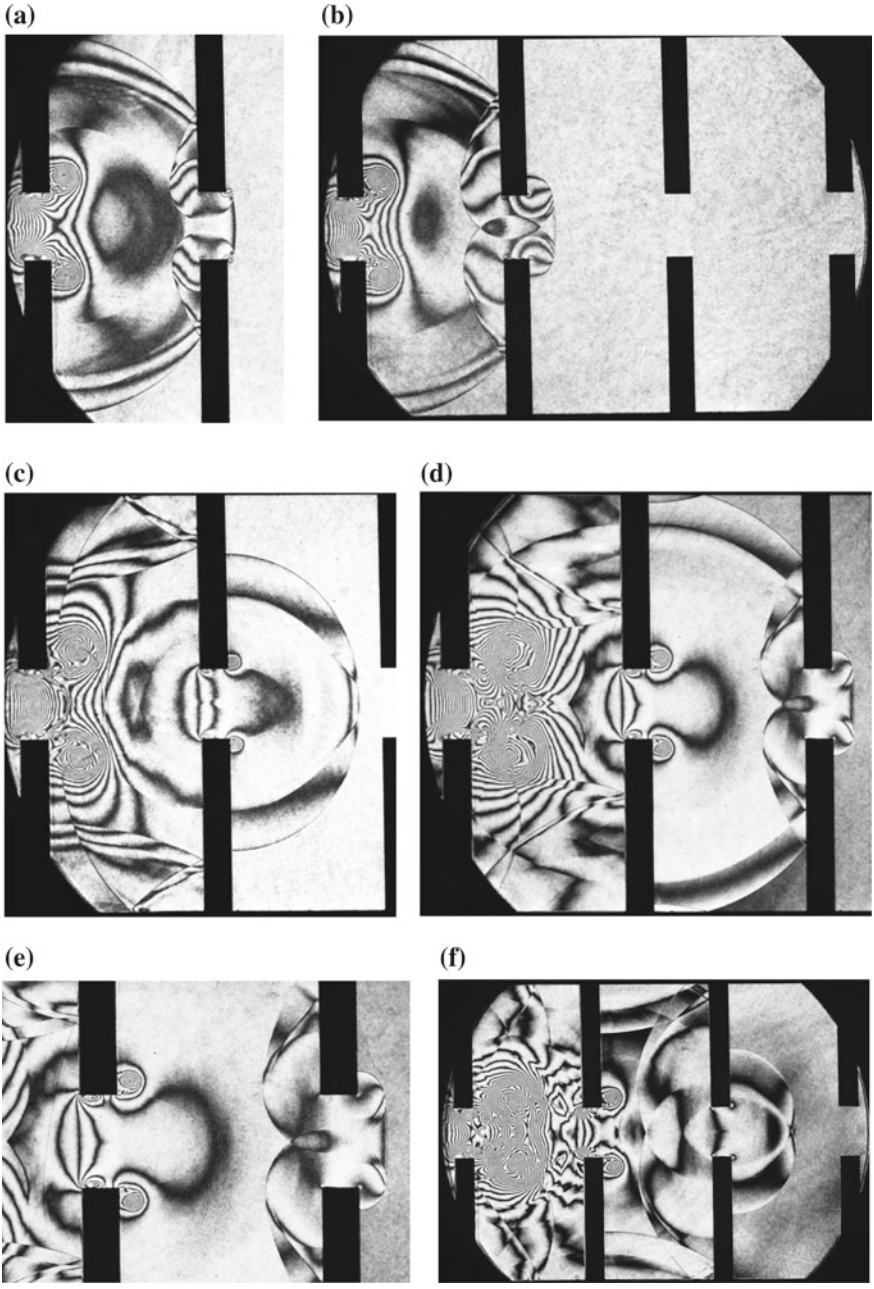


**Fig. 6.29** The shock wave propagation through a partition for Ms = 1.20 in air: **a** #97122505, Ms = 1.201; **b** #97122510, Ms = 1.194; **c** #97122503, Ms = 1.198; **d** #97122201, Ms = 1.193; **e** enlargement of (**d**); **f** #98010602, Ms = 1.196; **g** enlargement of (**f**); **h** #98010604, Ms = 1.203; **i** #98010605, Ms = 1.197; **j** enlargement of (**i**)

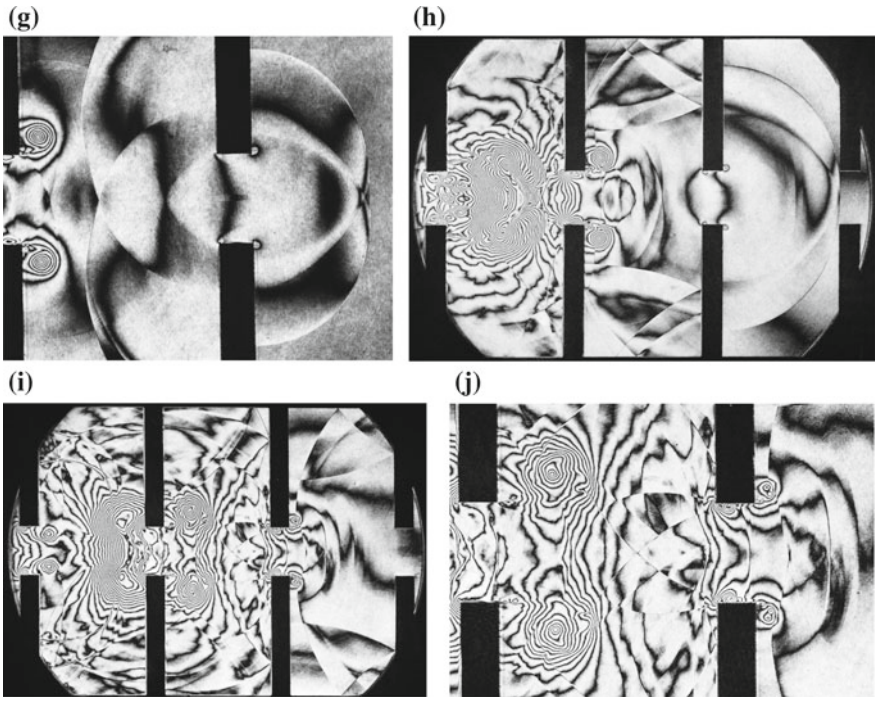


**Fig. 6.29** (continued)

twin vortices at the entrance. The vortices interacted with the reflected shock waves to result in complex wave interactions. This leads to the attenuation of the transmitted shock wave.

### *6.8.2 Cookie Cutter Entry and Exit*

The mufflers and silencers of automobile exhaust pipe lines were designed based mainly on acoustic theories. However, noises caused along the exhaust pipe lines were not necessarily acoustic noises but weak shock waves. Therefore, the acoustic theories are hardly effective. A partition having a staggered entrance and exist was installed in the 150 mm × 250 mm test section and sequentially visualized was conducted. In Fig. 6.30a–f, attenuation experienced by the transmitted shock wave passing through cookie cutter.

Figure 6.30f is an enlargement of Fig. 6.30e. The effect of cookie cutter on the shock wave attenuation was not promising because the sharp entrance shape would not effectively disturb the transmitted shock wave.

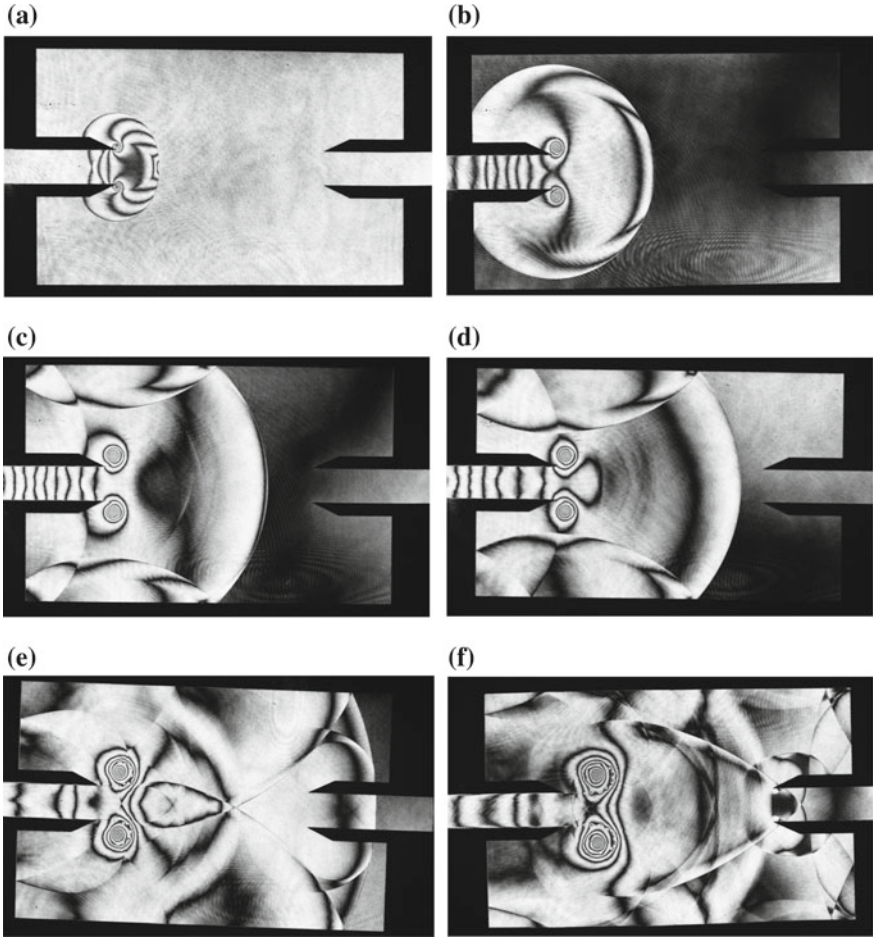


**Fig. 6.30** Shock wave entry into a partition having a cookie cutter entrance and exit for Ms = 1.15 in atmospheric air at 296.7 K: **a** #87093002, Ms = 1.154; **b** #87093003, Ms = 1.150; **c** #87093004, Ms = 1.153; **d** #87093005, Ms = 1.142; **e** #87093007, 750 μs, Ms = 1.150; **f** #87093008, Ms = 1.151

### *6.8.3 Staggered Cookie Cutter Entry and Exit*

The cookie cutter entry and exit were arranged in staggered manner. Experiments were conducted for Ms = 1.15 in atmospheric air at 296.7 K. The cookie cutter entry and exit did not contribute to significantly attenuate the transmitted shock wave but the staggered arrangement promoted attenuation. Figure 6.31a–h show shock wave attenuation in propagating in a full length partition having a staggered entry and exit for Ms = 1.15 in atmospheric air.

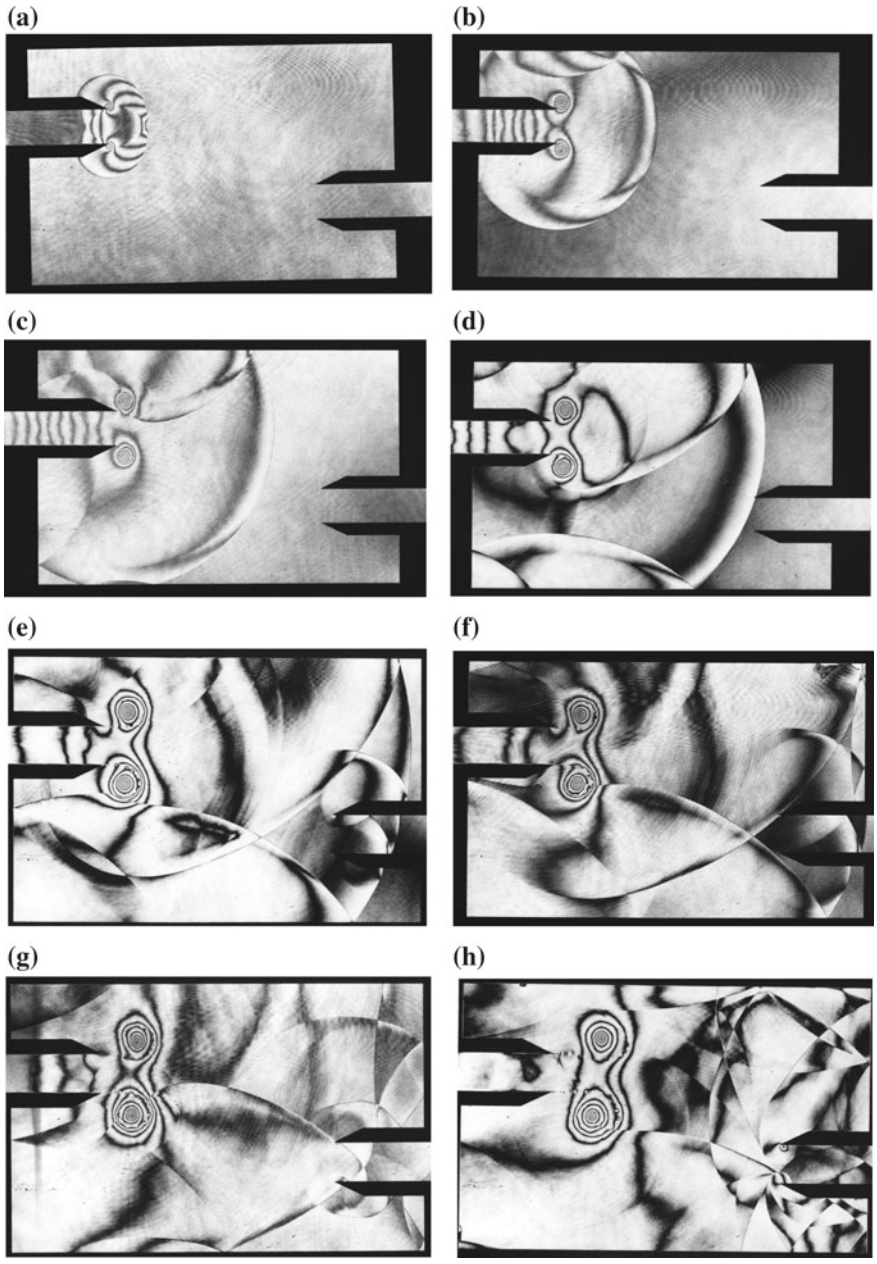


**Fig. 6.31** Shock wave entry into a partition with cookie cutter entrance and exit in staggered position for Ms = 1.15 in atmospheric air at 296.7 K: **a** #87093011, Ms = 1.147; **b** #87093012, Ms = 1.152; **c** #87093013, Ms = 1.149; **d** #87093014, Ms = 1.147; **e** #87093015, Ms = 1.155; **f** #87093016, Ms = 1.140; **g** 87093017, Ms = 1.148; **h** #87093019, Ms = 1.15

### 6.8.4 *Short Partition of Staggered Entry and Exit*

See Fig. 6.32a–f show shock wave attenuation in propagating in a half length partition having a staggered entry and exit for Ms = 1.13 in atmospheric air. Shock waves in this arrangement attenuated more effectively than that in the full length partition.

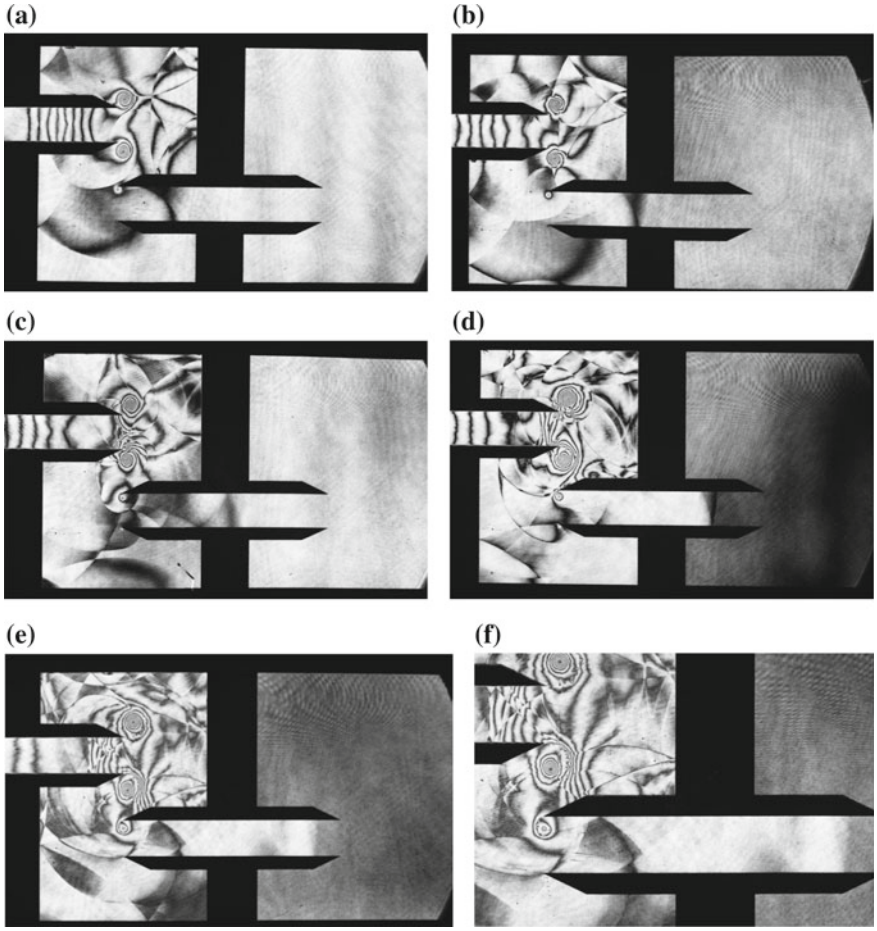


**Fig. 6.32** Shock wave entry into a short partition composed of cookie cutter entrance and exit in staggered position for Ms = 1.13 in atmospheric air at 296.7 K: **a** #87100101, 500 μs from trigger point; **b** #87100102, 550 μs; **c** #87100103, 600 μs; **d** #87100104, 650 μs, Ms = 1.14; **e** #87100105, 770 μs, Ms = 1.14; **f** enlargement of (**e**)

### 6.8.5 *Short Partition with Straight Entry and Oblique Exit*

Figure 6.33 show the shock wave interaction with a short partition having the blunt shape entrance and exit arranged in staggered position for Ms = 1.38 in

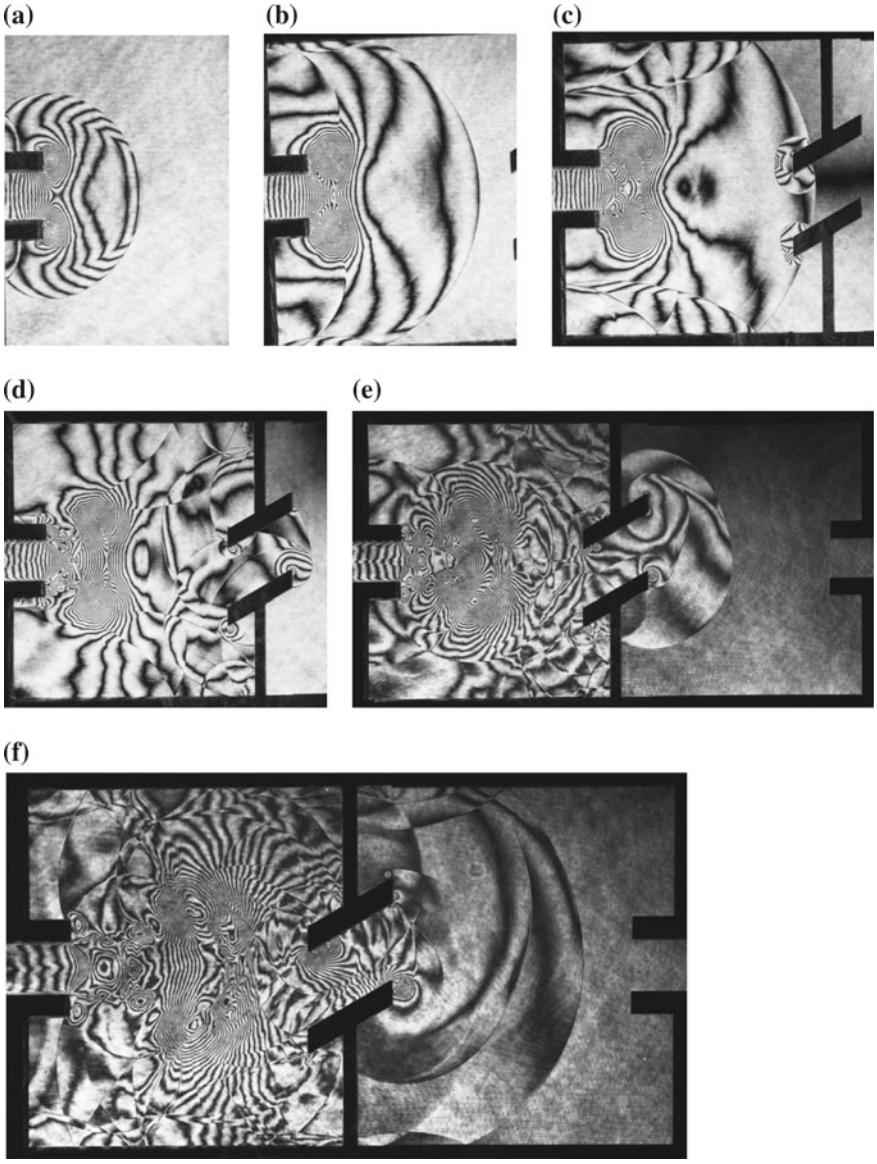


**Fig. 6.33** Shock wave entry into a short partition with the entrance and exit arranged in staggered position for Ms = 1.38 in atmospheric air at 294.2 K: **a** #92012010; **b** #92012011; **c** #92012012; **d** #92012013; **e** #92012014; **f** #92012015

atmospheric air at 294.2 K. The test pieces were installed in the 60 mm × 150 mm diaphragm-less shock tube. Blunt edges promoted diffraction and reflection of the transmitted shock waves and effectively attenuated the transmitted shock wave. It is clear from Fig. 6.33 shows that the transmitted shock wave passing the tilted exit is attenuated.

### 6.8.6 *Upright Baffle Plates*

In a synchrotron radiation facility, intense synchrotron radiation is mitted by irradiations of high-energy beams on a thin beryllium plate. Then, the beryllium plate separates an ultra high-vacuum ring from the ambient air. In case the beryllium plate accidentally ruptured, the atmospheric air rushed into the ring. Then rushed air would break not only the high-vacuum but also contaminate the surface of the structures inside the ring (Ohtomo 1998).

Taking the pressure ratio of air in the ambient condition and the ultra-high-vacuum condition into account, this arrangement is analogous to a shock tube having very high pressure ratio. Therefore, the beryllium plate rupture creates a high speed air flow which is equivalent to a contact surface in the shock tube flows and drive a strong shock wave. The gate valve is equipped in a beam line, a duct connecting the ring and the beryllium plate, and is intended to immediately stop the shock wave and the contact surface in case the beryllium plate ruptured; it is important to retard the shock wave and contact surface arriving at the gate some time before the gate valve was closed. Usually, skimmers are arranged in a row along the beam line. The skimmers work as partition plates.

In the recorded interferograms, obliquely entering shock waves attenuated faster than those entering upright shock waves much more effectively than the upright entry. Therefore, even if it is a two-dimensional experiment, the effectiveness of oblique baffle plates would be verified testing it in the 180 mm × 1100 mm test section of the 100 mm × 180 mm diaphragm-less shock tube. Figure 6.34a, b show the test section of the refurbished UTIAS hypervelocity shock tube and the combination of four pieces of 250 mm × 250 mm plane mirrors, which formed 250 mm × 1000 mm mirror (Ohtomo 1998).

Figure 6.35 show the evolution of the shock wave propagating along an upright arrayed baffle plates for Ms = 3.0. The shock wave propagates from right to left and the tip of the upright baffles were sharpened. The field of view height vi is 180 mm and the opening width is 20 mm. Pressure transducers (Kistler 603B) were placed marked from a to h. Figure 6.35a shows that the diffracting shock wave is going to interact successively with the attenuating baffle plates. Leaving from the last baffle plate, the transmitted shock wave attenuated significantly as seen in the pressure history measured at port f in Fig. 6.35f. In Fig. 6.35h, the ordinate denotes dimension less pressure normalized by the ambient pressure. The abscissa denotes the elapsed time in μs. Blue line shows the IS pressure at t = 0. Red and green lines

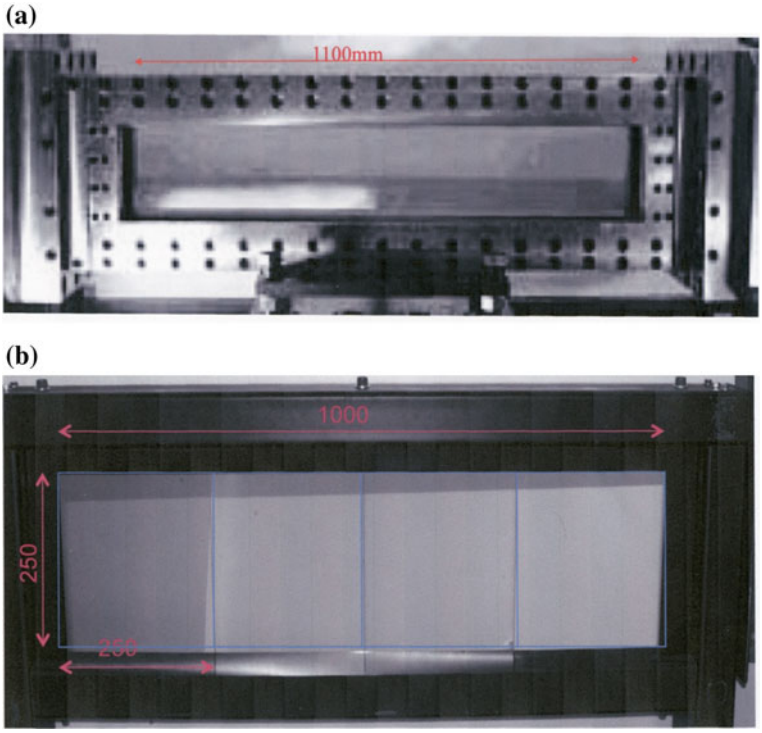


**Fig. 6.34** The 1100 mm × 180 mm test section connected to the refurbishes 100 mm × 180 mm shock tube: **a** 180 mm × 1100 mm test section; **b** combination of four pieces of 250 mm × 250 mm plane mirrors (Ohtomo 1998)

denote appropriate numerical simulation (Voinovich et al. 1998) and measured data, respectively. They agree well with each other.

### *6.8.7 Staggered Baffle Plates*

Figure 6.36 show the sequence of shock wave propagation along oblique baffle plates arranged staggered arrangement for Ms = 3.0 in air. The transmitted shock wave and the following contact region propagate along a zig-zag course. Figure 6.36a shows the staggered baffle plate arrangement and distribution of pressure measure by a transduces Kistler 603B.

Figure 6.36g shows the recorded pressure history measured at the port d by Kistler 603B. The ordinate denotes dimension-less pressure normalized by ambient pressure. The abscissa denotes the elapsed time in μs. Blue line denotes the incident shock pressure measure at t = 0. Red and green lines denote the numerical

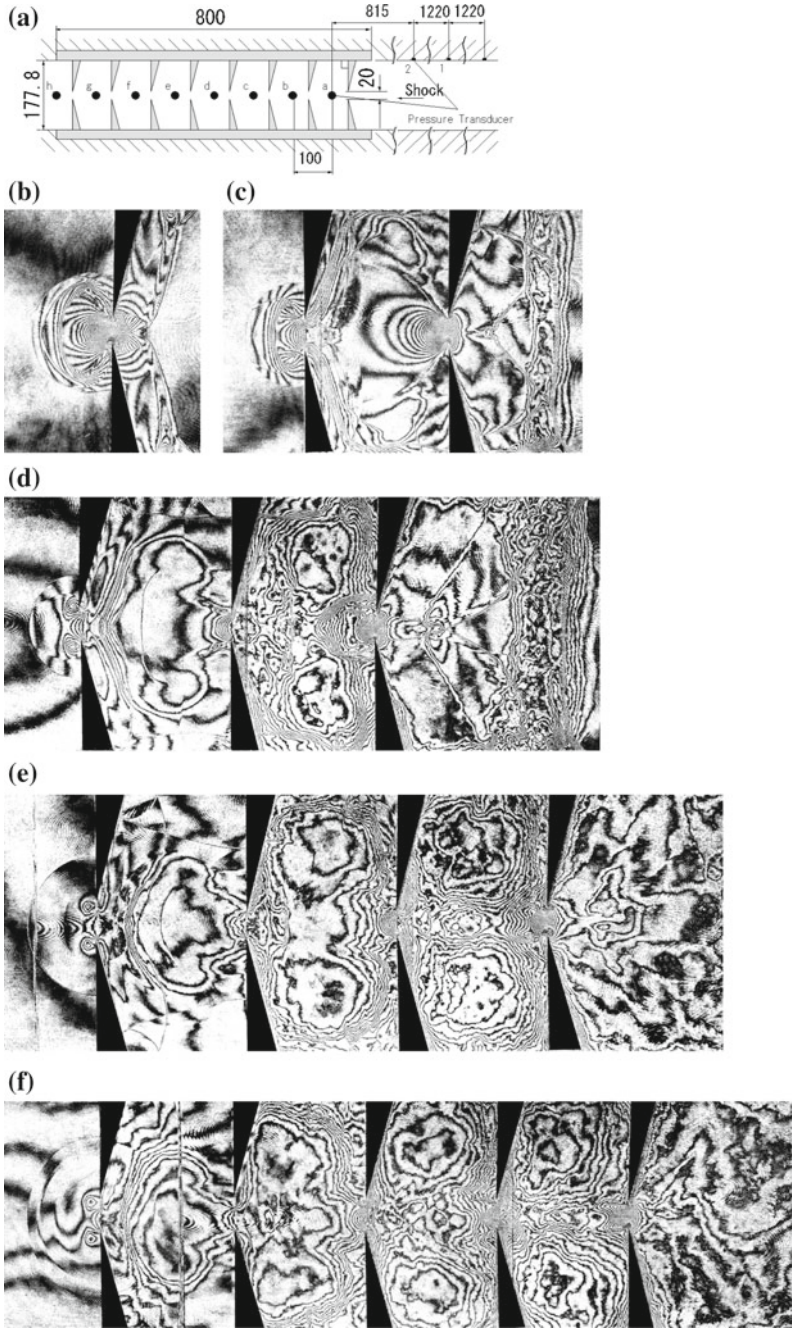


**Fig. 6.35** The evolution of the shock wave attenuation along upright baffle plates for Ms = 3.0 in air: **a** baffle plate arrangement; **b** #02111103; **c** #02111104; **d** #02111102; **e** #02111101; **f** #0211010; **g** #02111106; **h** pressure history at the port (**f**) (Ohtomo 1998)

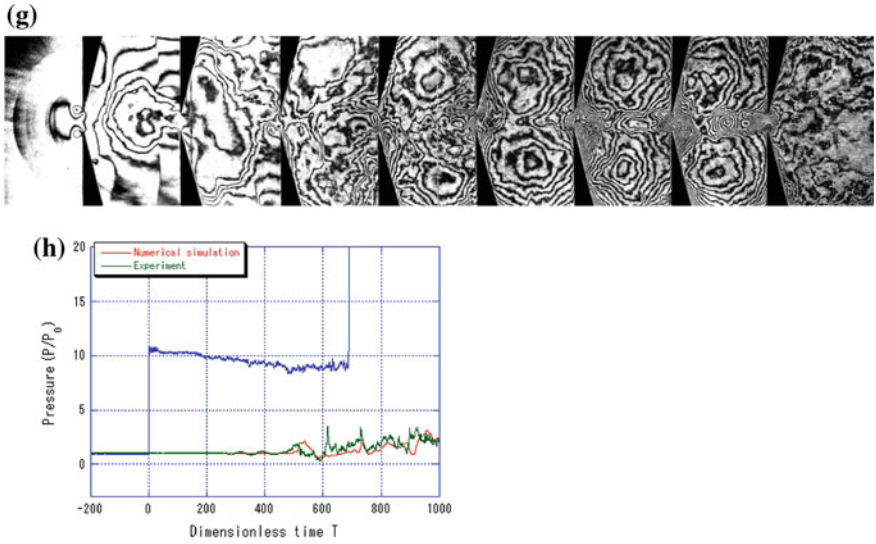


**Fig. 6.35** (continued)

simulation and the measured pressure distribution, respectively. The numerical result agrees well with the measured ones.

Comparison of the present pressure history with the one shown in Fig. 6.35h, readily indicates that the oblique baffle plate arrangement effectively attenuated the transmitted shock waves. In conclusion, crossing obliquely arranges skimmers, gas particles would take a zig-zag course and then the contact surface would be slowed down resulting in effectively attenuating the passing shock wave.

### *6.8.8 Numerical Comparison Between Upright and Staggered Oblique Baffle Plates*

The effect of the baffle plate alignments on the transmitted shock wave was investigated solving the Euler equations for incident shock Mach number Ms = 1.5 in ideal diatomic gas (Voinovich et al. 1998). Obtained results revealed that a staggered oblique array of baffle plates attenuated the transmitted shock wave and slowed down the contact region motion significantly better than the similar upright baffle plates. Figure 6.37a–d show numerically constructed interferograms of shock wave propagation along an array of the upright baffle plates as well as numerical results of an array of the staggered oblique It should be noticed that baffle plates' edge had a blunt end.

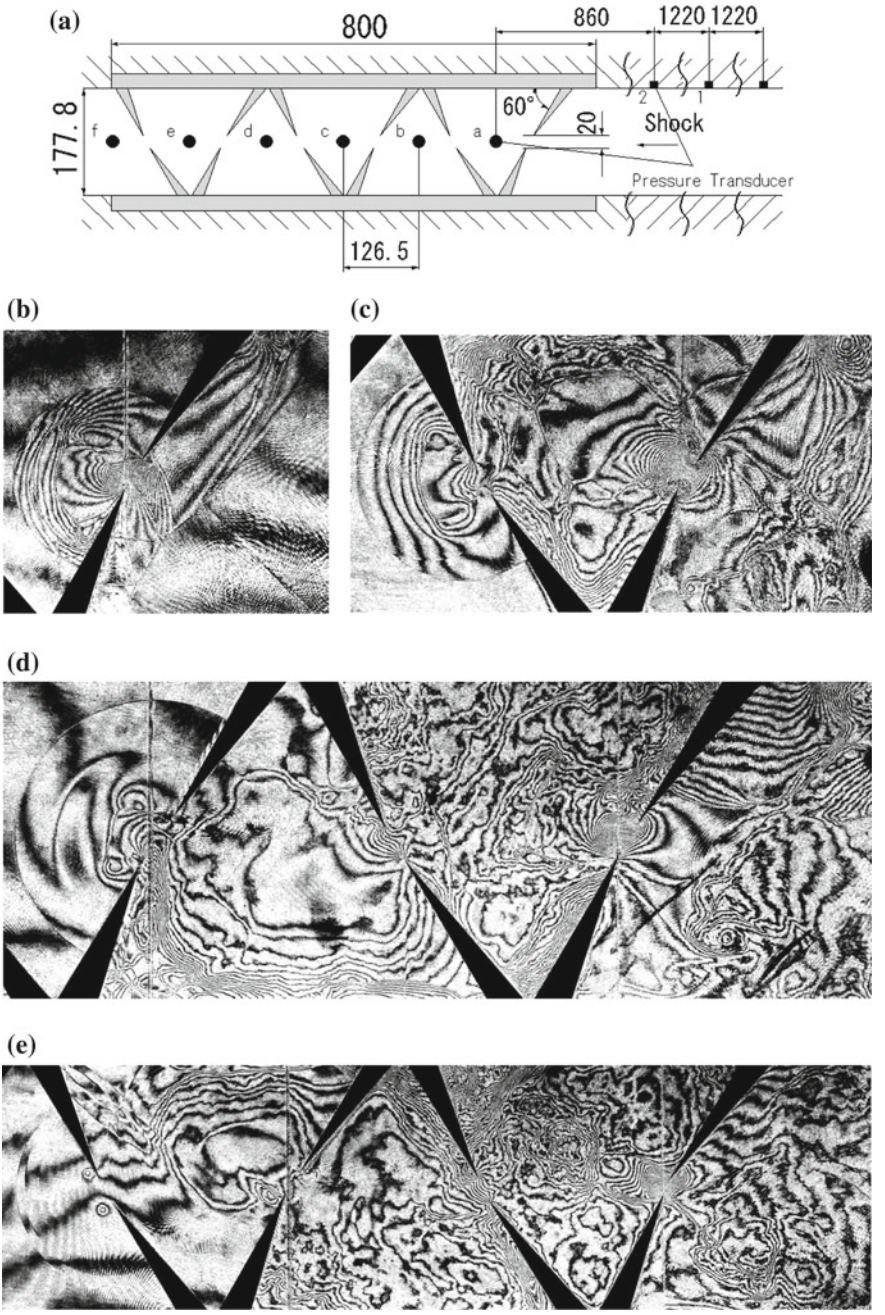


**Fig. 6.36** The shock wave attenuation along staggered baffle plates for Ms = 3.0 in air: **a** baffle plate arrangement; **b** #02111108; **c** #02111107; **d** #02111109; **e** #02111105; **f** #02111111; **g** pressure history measured at the port (**d**) (Ohtomo 1998)

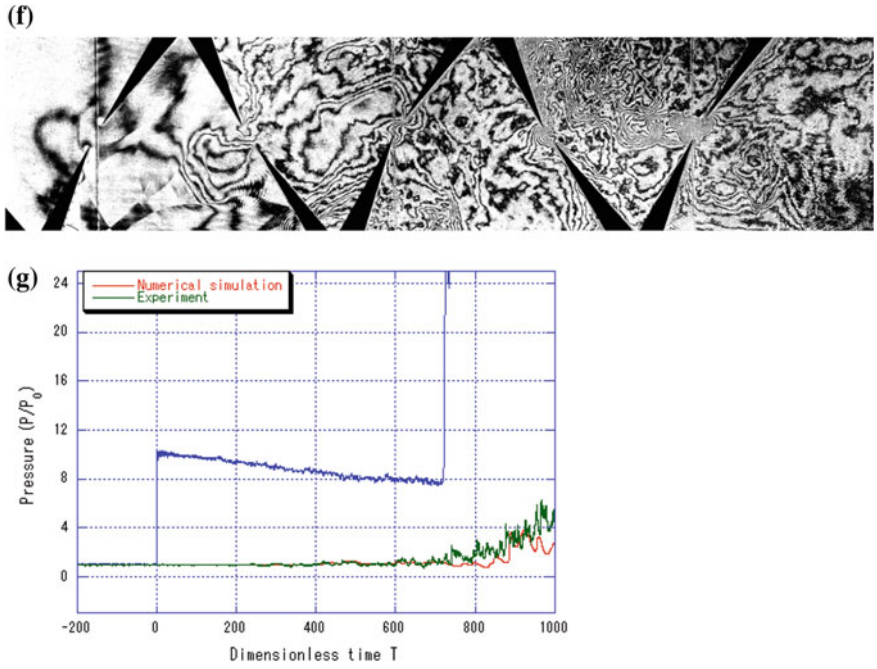


**Fig. 6.36** (continued)

## 6.9 Shock Wave Propagation Along a Double Elbow

In order to experimentally investigate the shock wave propagation through relatively complex duct's geometries, the flow through a double elbow would be an appropriate topic as shock wave propagations along an elbow was already studied (Takayama 1993).

### *6.9.1 Double Elbows Having Smooth Surface*

Figure 6.38 show the evolution of shock wave propagation through a double elbow duct having smooth surfaces for Ms = 1.21 in atmospheric air at 294 K. This is, in principle, a combination of two elbows. The incident shock wave was diffracted at the first entrance corners and repeated the diffraction at the second and the third corners. The transmitted shock wave was reflected from the first outside corner and repeated reflection at the second inside corner. The reflected shock waves interacted with the diffracted shock wave. The evolution of the shock wave propagation, eventually, became complex enough to make experimentalists amuse and to use numerical simulation to reproduce the prevailing flows. The transmitted shock wave attenuated when it exits the duct as seen in Fig. 6.38e.

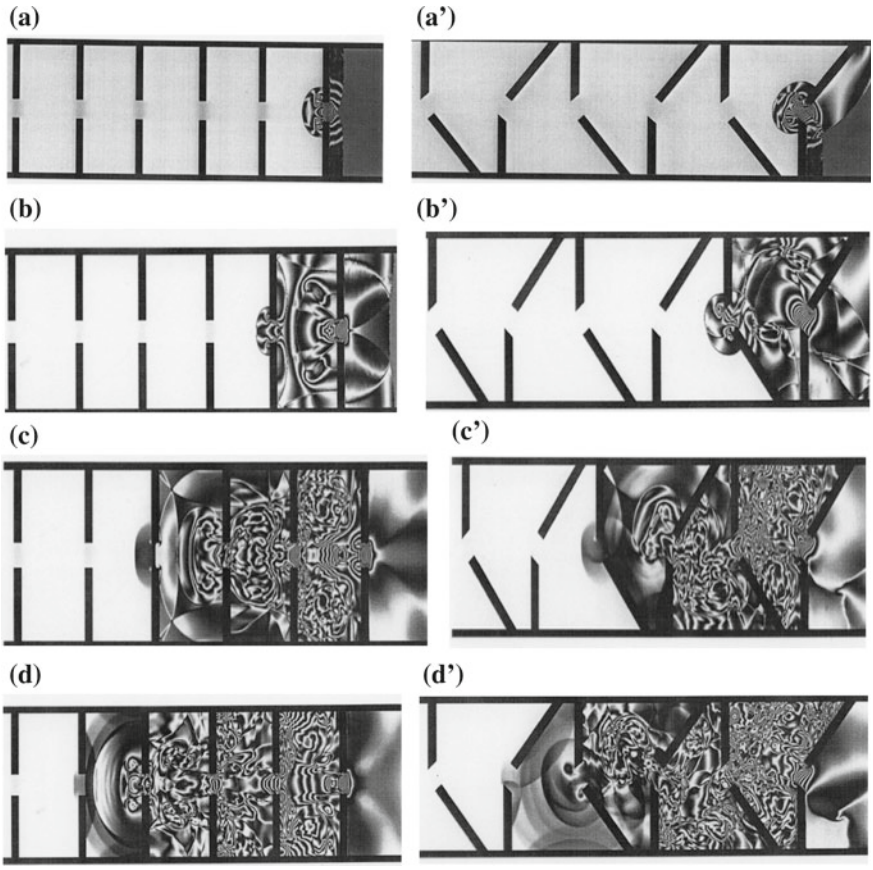


**Fig. 6.37** Numerical comparison of shock wave mitigation between upright and staggered baffle plates for Ms = 1.5 in air (Voinovich et al. 1998)

### *6.9.2 Double Elbows Having Roughened Surface*

As seen in Fig. 6.13, the shock wave was effectively attenuated through roughened surface. Figure 6.39 show the evolution of shock wave propagating along the double elbow having the same surface roughness as seen in Fig. 6.13. The double elbow having roughened surface attenuated the transmitted shock waves much more efficiently than that having smooth surface.

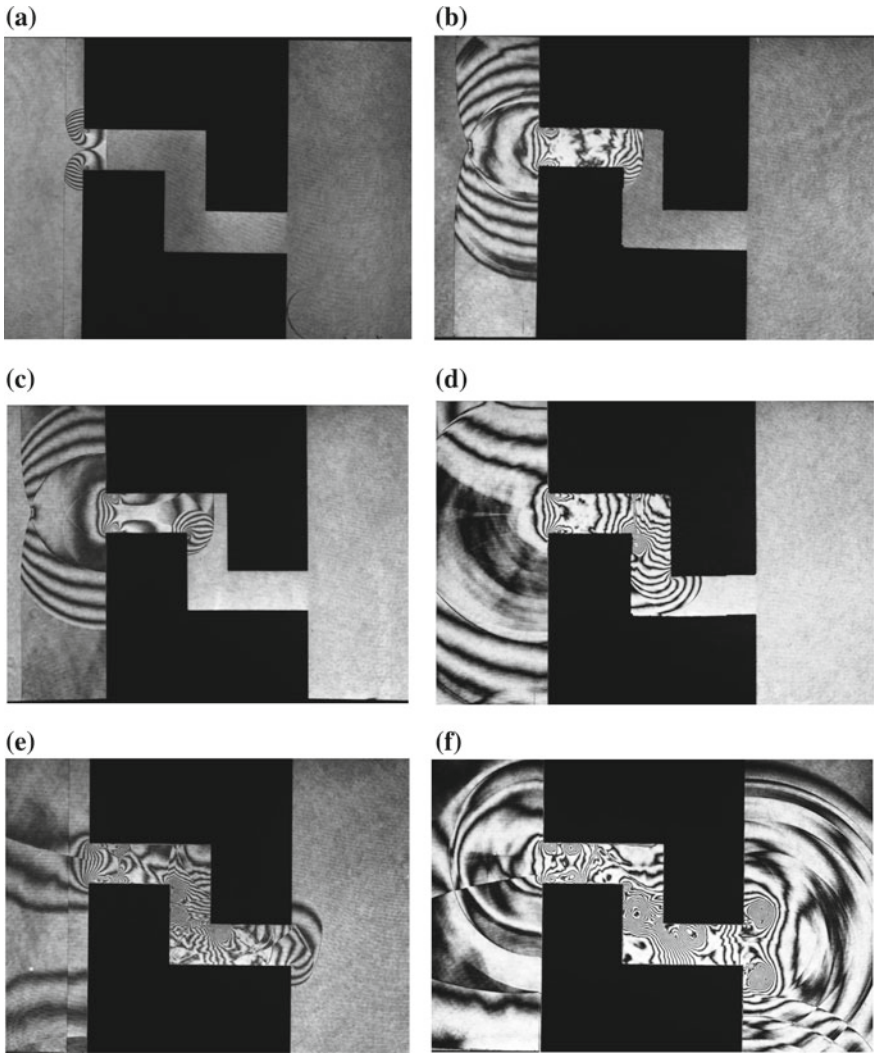


**Fig. 6.38** The shock wave propagation through a double elbow having a smooth surface for Ms = 1.21 in atmospheric air at 294 K: **a** #93042001, 400 μs, Ms = 1.221; **b** #93042110, 500 μs from trigger point, Ms = 1.214; **c** #93042002, 500 μs, Ms = 1.220; **d** #93042111, 600 μs, Ms = 1.221; **e** #93042004, 700 μs, Ms = 1.219; **f** #93042006, 900 μs, Ms = 1.225

## 6.10 Arrayed Cylinders and Spheres

It is known that the train tunnel sonic booms released from tunnels having a gravel track are less-louder than those released from tunnels having a concrete floor or the so-called slab track. This difference is physically based on the fact that the gravel

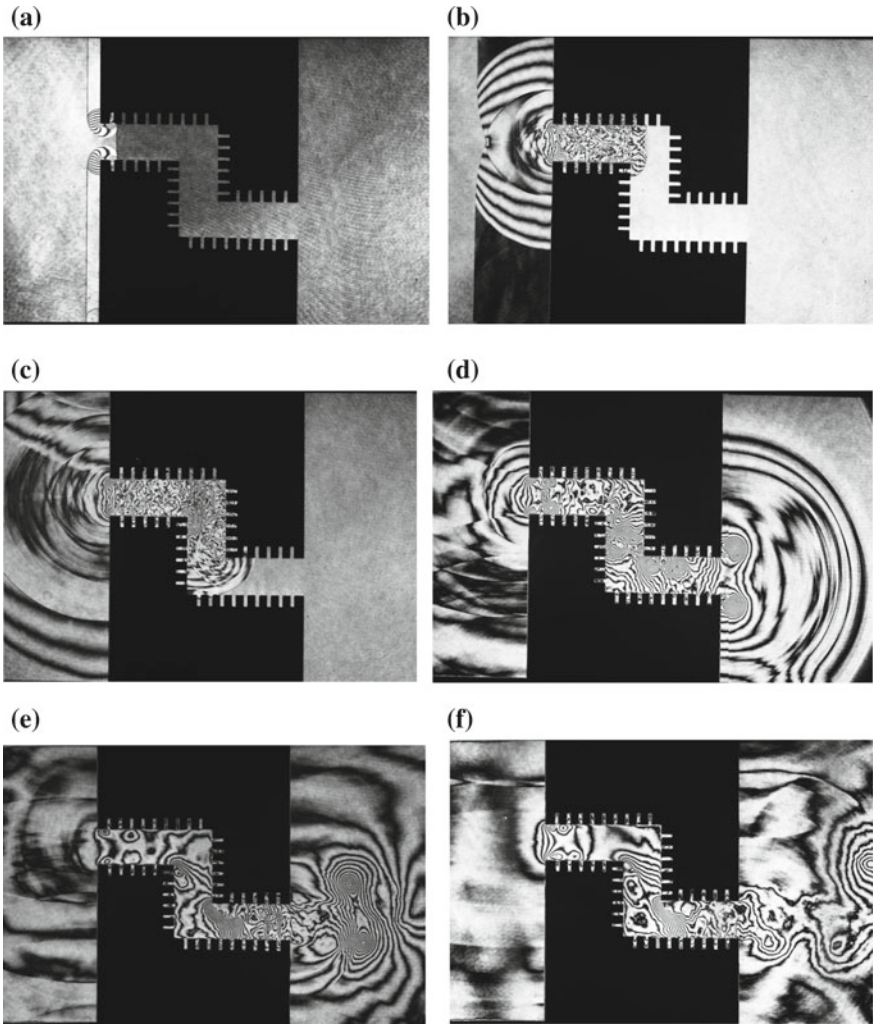


**Fig. 6.39** Shock wave mitigation over a double elbow with perforations at Ms = 1.22 in air at 1013 hPa, 294 K: **a** #93042108, 400 μs from trigger point Ms = 1.219; **b** #93042107, 500 μs, Ms = 1.211; **c** #93042106, 600 μs, Ms = 1.215; **d** #93042103, 900 μs, Ms = 1.217; **e** #93042102, 1300 μs, Ms = 1.217; **f** #93042101, 1800 μs, Ms = 1.218

track is, in short, a layer of gravels and readily attenuates booms much more efficiently than the slab track.

During the operation of the Japan's first high-speed train network, no one claimed the train tunnel sonic booms. However, the high-speed train network was expanded to the southern Japan and the train speed was increased, people started to claim the train tunnel sonic booms. All the first generation train tunnels had gravel tracks, whereas all the upgraded train tunnels constructed in the second generation

had slab tracks. The sonic booms were caused by the difference of the track's support. This became a motivation of the present series of experiments.

In an analogue experiment, the sequence of shock wave propagation along the arrayed cylinders or spheres was planned. At first the investigation was aimed at the visualization of shock wave propagating through three-dimensionally packed gravels. However, it was not a simple to reproduce such a situation by arranging spheres in three-dimensional space. Alternatively, an easy case was examined. Three 22 mm diameter spheres were connected in a line by truncated their edge and formed into 56 mm and installed the 60 mm × 150 mm diaphragm-less shock tube. The arrangement was shown in Fig. 6.40. Images of the shock wave propagation over these spheres were compared with that over 30 mm diameter cylinders (Abe 2002).

Figure 6.41 show the evolution of shock wave propagation along 30 mm diameter arrayed cylinders for Ms = 1.10 in atmospheric air at 293.5 K. As the reproducibility of experiments were good, then sequential observation using shorter delay time enabled to arrange the resulting interferograms in an animated display.

Figure 6.42 show the evolution of shock wave propagation along 30 mm diameter arrayed cylinders for Ms = 1.30 in air at 560 hPa, 289.5 K. A shock wave diffraction over a single cylinder was already discussed in Fig. 4.2. The diffraction and reflection occurred repeated as seen in Fig. 6.42b and its enlargement in Fig. 6.42c. The degree of the interaction among the transmitted shock waves became very complex. Then as already discussed, at every step when the transmitted shock waves passed the line of the cylinders, the fringe distribution behind the leading transmitted shock wave became complicated as seen in Fig. 8.35f.

Figure 6.43 show the evolution of shock wave propagation along 25 mm diameter arrayed spheres for Ms = 1.10 in atmospheric air at 295.5 K. The total projected area of the arrayed spheres to the shock tube cross section, the so-called

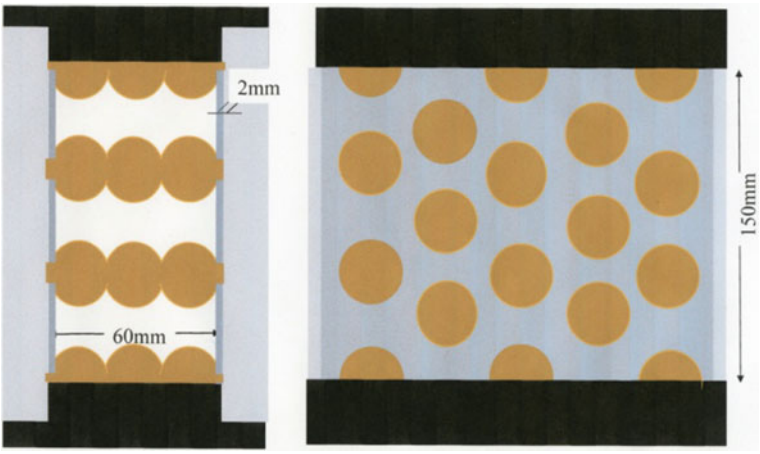


**Fig. 6.40** Arrayed spheres installed in the 60 mm × 150 mm diaphragm-less shock tube

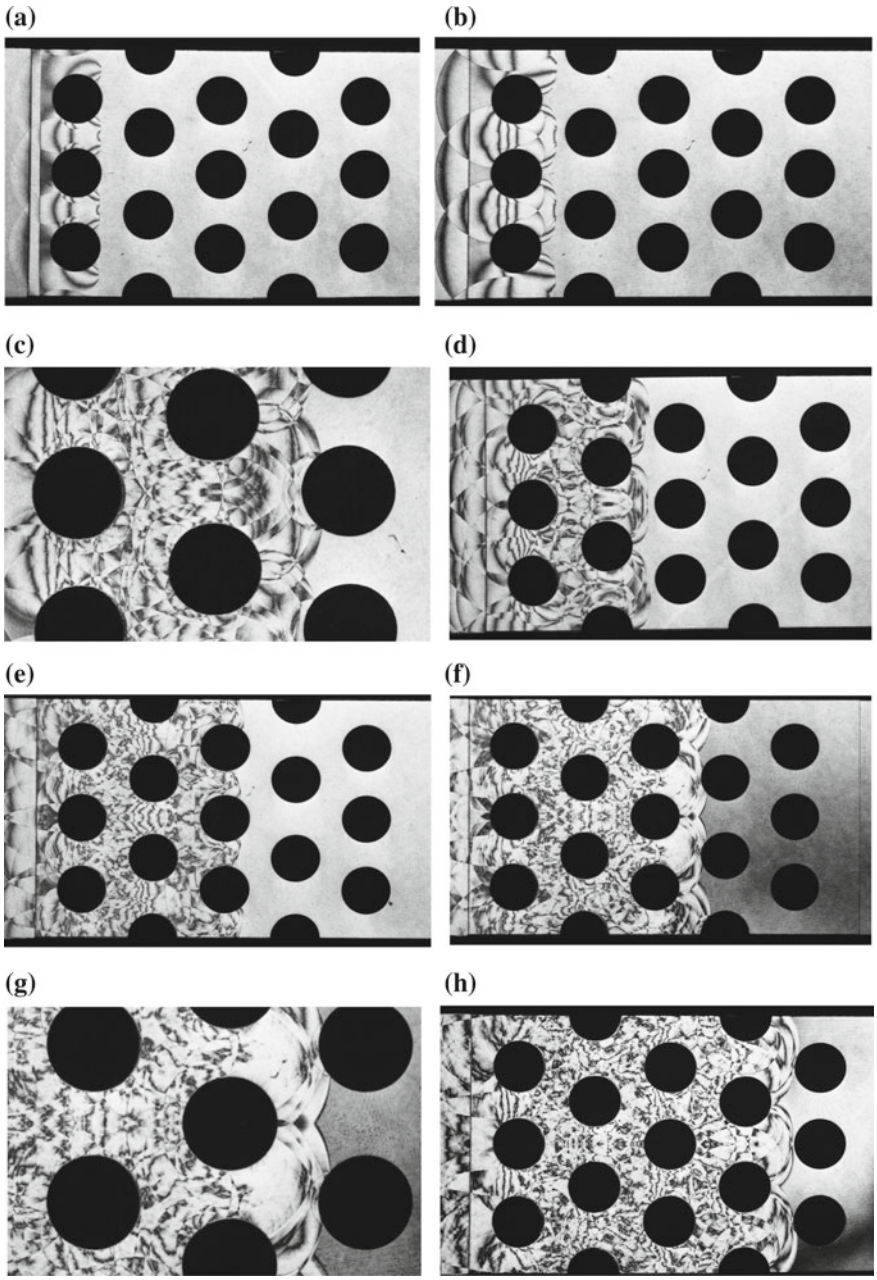


**Fig. 6.41** Shock wave attenuation along an array of 30 mm diameter cylinders for Ms = 1.10 in atmospheric air at 293.5 K: **a** #98010910, 87 μs from the shock wave arrival at frontal stagnation point, Ms = 1.110; **b** #98010913, 116 μs, Ms = 1.104; **c** #98010908, 263.7 μs, Ms = 1.115; **d** #98010915, 245.5 μs, Ms = 1.104; **e** #98010909, 304.5 μs, Ms = 1.110; **f** #98010912, 381.8 μs, Ms = 1.103; **g** #98010912, Ms = 1.103; **h** #98010923, 497.1 μs, Ms = 1.111

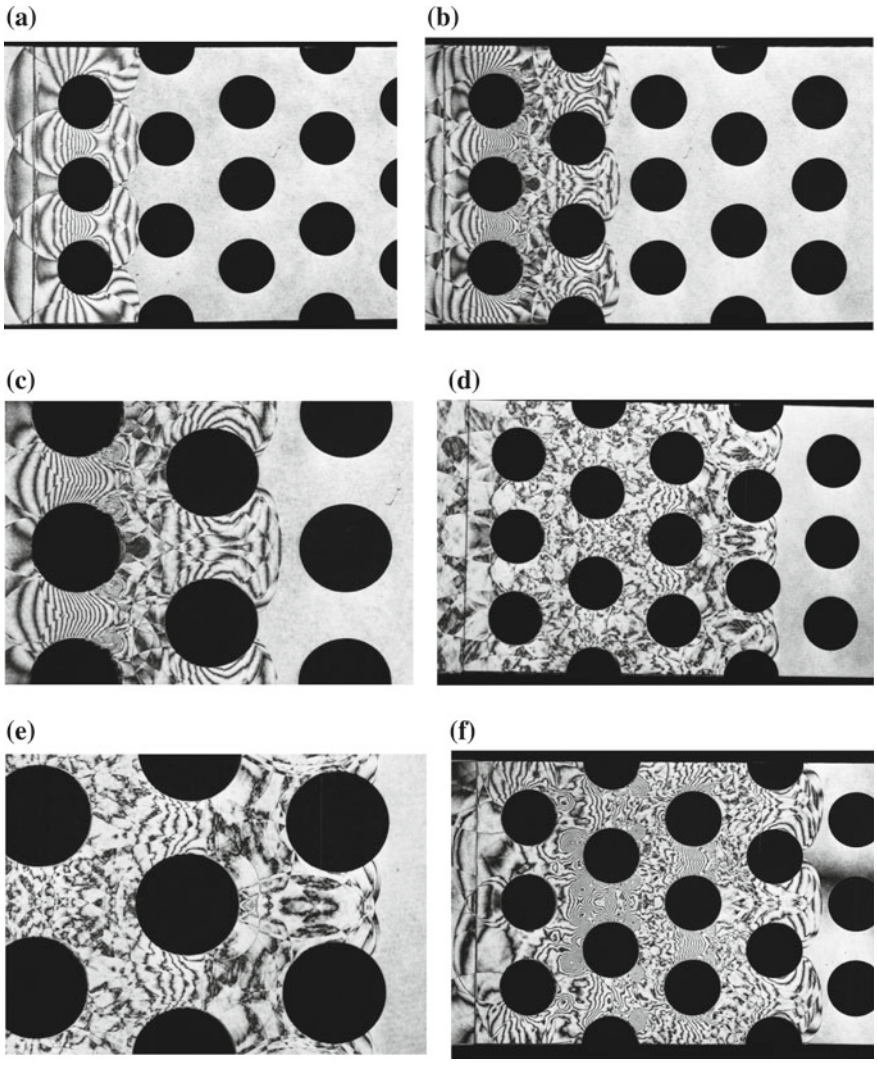


**Fig. 6.42** Shock wave attenuation along an array of 30 mm diameter cylinders for Ms = 1.30 in air at 560 hPa, 289.5 K: **a** #98011205, 100 μs, Ms = 1.301; **b** #98011201, 184.3 μs, Ms = 1.298; **c** enlargement of (**b**); **d** #98011204, 346.4 μs, Ms = 1.294; **e** enlargement of (**d**); **f** #98011215, 364.5 μs, Ms = 1.306

the blockage ratio is 54% as seen in Fig. 6.43, whereas it is 63% for cylinders as seen in Fig. 6.42. In the interaction of a planar shock wave with a single sphere, the feature of the transmitted shock waves is different from the interaction of a planar shock wave with a single cylinder. Although the array of spheres are slightly similar to the case of arrayed cylinders, the fringe distributions observed in Fig. 6.43f look much more complicated than those observed in Fig. 6.42f.

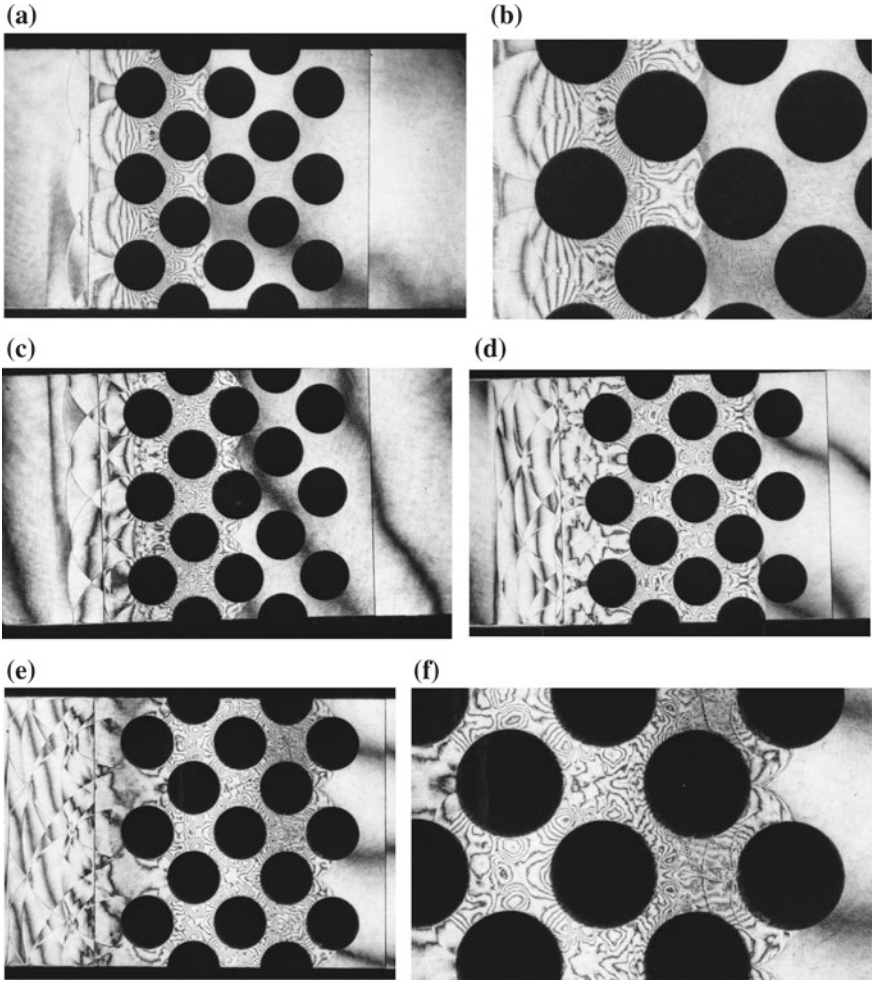


**Fig. 6.43** Shock wave attenuation along an array of 22 mm diameter spheres for Ms = 1.10 in atmospheric air at 295.5 K: **a** #99102916, 575 μs from trigger point, Ms = 1.099; **b** enlargement of (**a**); **c** #99102917, 195 μs, Ms = 1.115; **d** #99102918, 272.5 μs, Ms = 1.099; **e** #99102920, 312.0 μs, Ms = 1.115; **f** enlargement of (**e**)

Figure 6.44 show an animated display of arrayed five 22 mm diameter spheres for Ms = 1.10. Sequential interferograms are edited for making an animated display. The blockage ratio of this particular arrangement is 75%. In this arrayed sphere five spheres were installed in a line, whereas four spheres were arranged in Fig. 6.43, therefore, the blockage ratio was 54%. The fringe distributions behind the leading shock wave became simpler with elapsing time as observed in Fig. 6.44r.

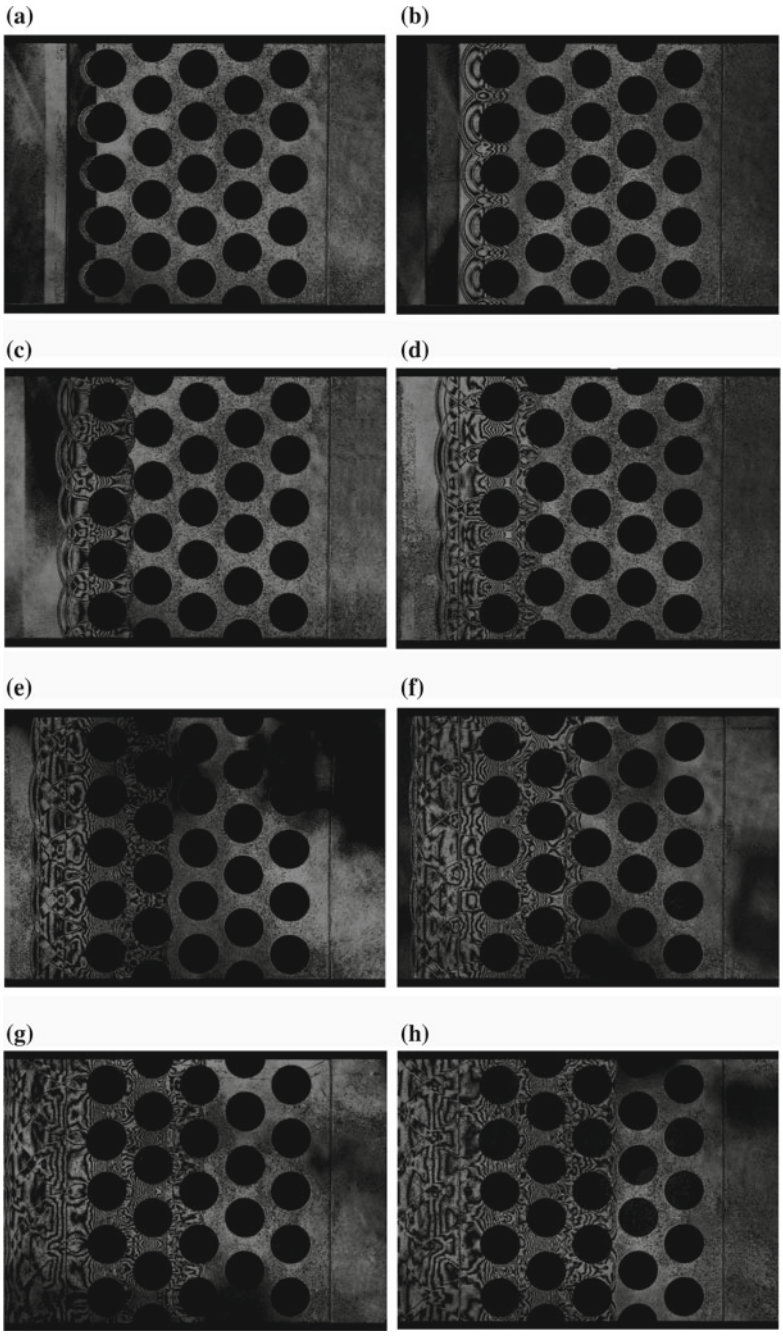


**Fig. 6.44** Animated display of shock wave propagation along arrayed spheres, #99102901 for Ms = 1.10, 22 mm diameter spheres (Abe 2002)

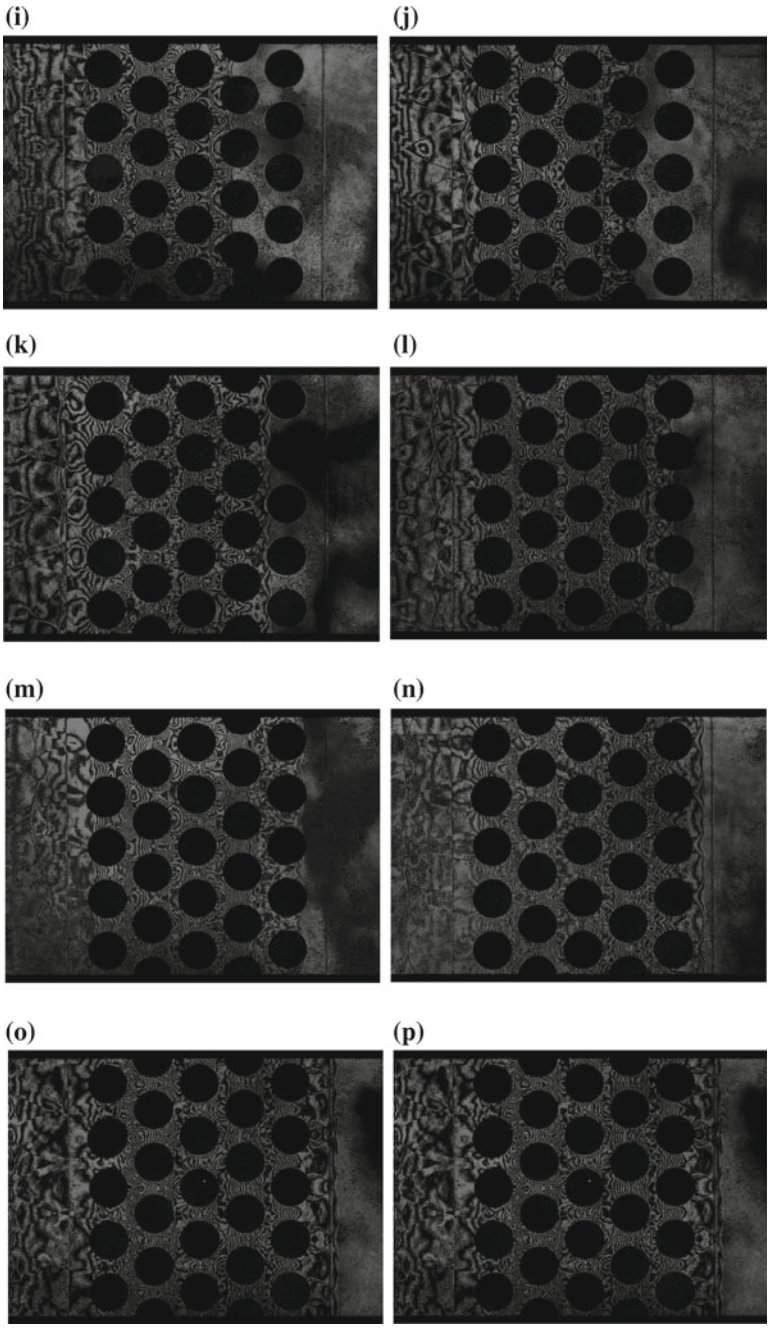


**Fig. 6.44** (continued)

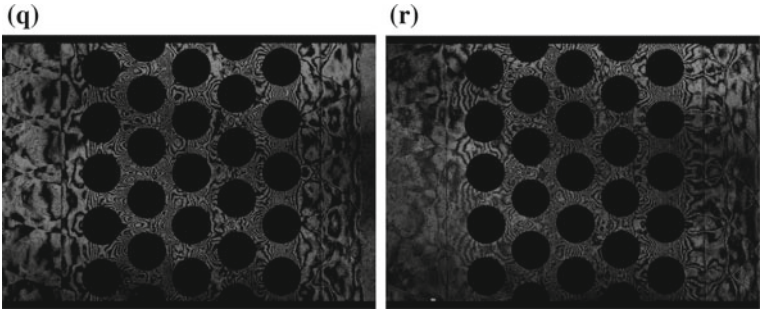


**Fig. 6.44** (continued)

## 6.11 Shock Waves Released from Trailing Edges

When a shock wave passes along a slender body whose upper surface and lower surface have different surface roughness, the shock waves on the upper surface and lower surface would have different strength. If these shock waves are released from the trailing edge as shown in Fig. 6.38, a vortex will be formed some time after an elapsed time.

### *6.11.1 Vortex Formation*

A 500 mm long splitting plate was inserted along the center line of the 60 mm 150 mm diaphragm-less shock tube. The trailing edge was positioned at the entrance of the test section as seen in Fig. 6.45. The upper part of the splitting plate

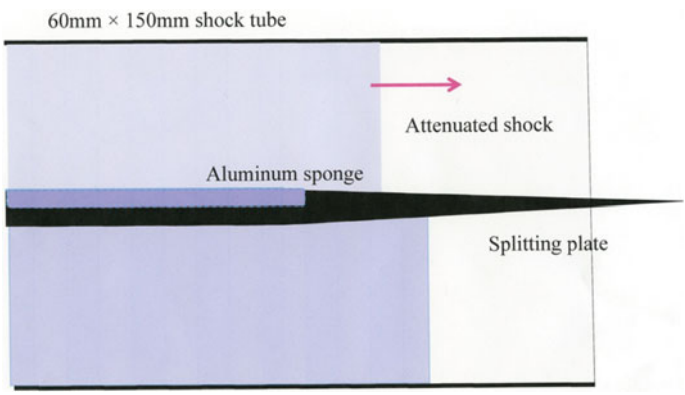


**Fig. 6.45** A vortex released from a trailing edge of the 60 mm × 150 mm diaphragm-less shock tube

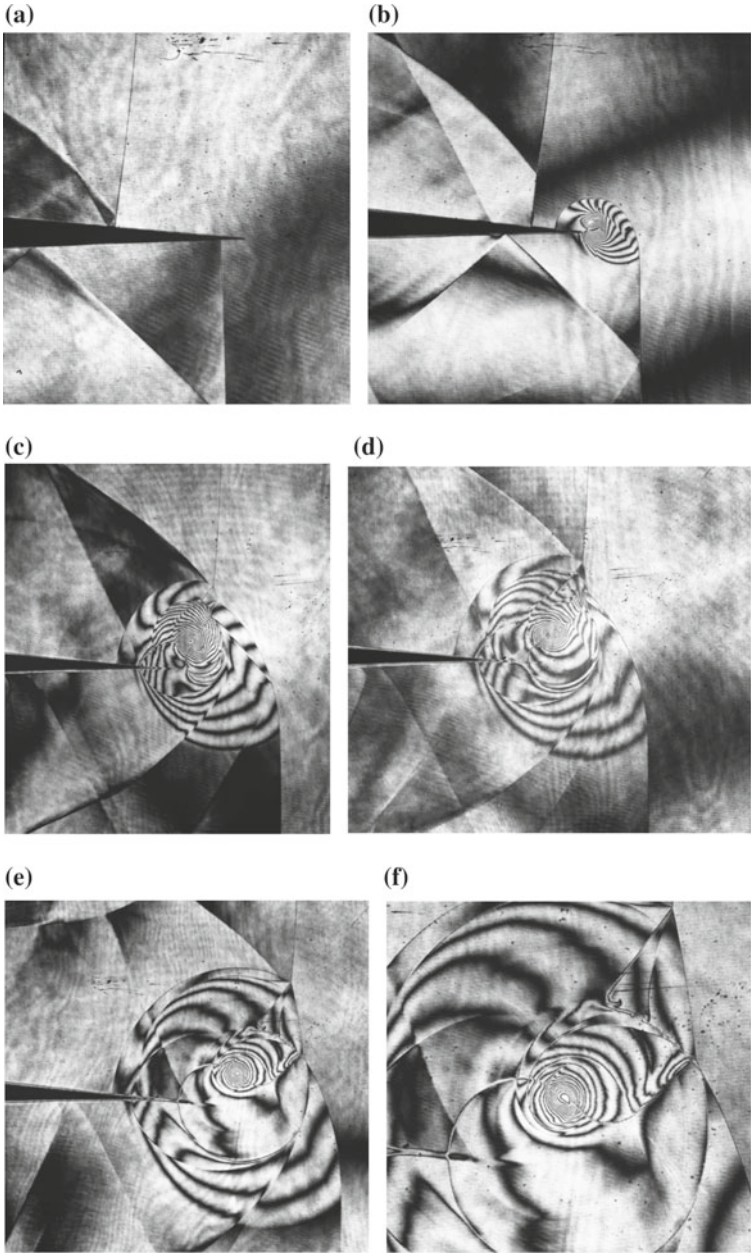


**Fig. 6.46** Vortex formation at a splitting plate trailing edge. A metal form was installed on the upper side of the splitting plate for attenuating the shock wave propagating along the upper side for Ms = 2.2 in air at 300 hPa, 288.5 K: **a** #88021003, 635 μs from trigger point, Ms = 2.176: **b** #88021002, 670 μs, Ms = 2.183; **c** #88020909, 715 μs, Ms = 2.152; **d** #88020908, 730 μs, Ms = 2.159; **e** #88020907, 745 μs, Ms = 2.193; **f** #88020907, 745 μs, Ms = 2.193; **g** #88020904, 0.8 ms, Ms = 2.263; **h** #88020904, 0.8 ms, Ms = 2.263; **i** #88020903, 840 μs, Ms = 2.177; **j** #88020902, 1.9 ms, Ms = 2.193

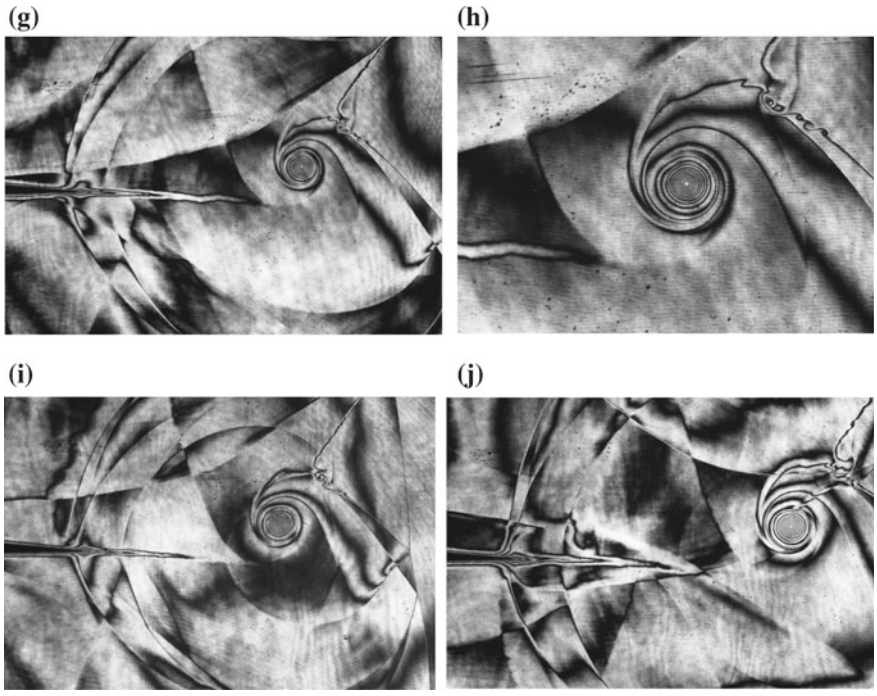


**Fig. 6.46** (continued)

had a 200 mm long aluminum sponge so that the shock wave propagating along the upper surface would be attenuated. However, the shock wave propagating along the lower surface would remain at the same speed. The splitting plate worked to generate a shear flow behind the transmitted shock waves. Then some time later, a vortex would appear at the trailing edge. Figure 6.45 shows the experimental arrangement.

Figure 6.46 show the evolution of the vortex formation at the trailing edge for incident shock Ms $\approx$ 2.2 in air at 300 hPa, 288.5 K. The particle speed behind the transmitted shock wave is supersonic and that along the lower surface is about 10% faster than that along the upper surface. At first, a complex diffraction occurs at the trailing edge as seen in Fig. 6.46b. The diffracting shock wave initiates a distinct vortex. The vortex develops at elapsed time is seen in Fig. 6.46b–d. The vortex gradually depart from the trailing edge as seen in Fig. 6.46e–j.

### 6.11.2 Vortex Formation from a Two-Dimensional Separator

Replacing the sharp trailing edge as seen in Fig. 6.46 with a 50 mm wide two-dimensional backward facing splitting plate resulted in a different the vortex formation. Figure 6.47 show the evolution of diffraction at backward facing corner for Ms = 1.24 in atmospheric air at 292.8 K. At Ms = 1.24, even if the flow at the corner is accelerated, the corner flow remains subsonic and the boundary layer developed along the splitting plate is separated from the corner as seen in Fig. 6.47c–g.

### 6.11.3 Asymmetric Two-Dimensional Splitting Plate

Figure 6.48 show the evolution of asymmetric interaction of transmitted shock waves released from 50 mm wide splitting plate for Ms = 1.50 in atmospheric air at 294.2 K. At this value of Ms, the flow at the corner is accelerated and eventually becomes supersonic. Distributing the roughness along the lower surface, the shock wave propagating over it is attenuated. Therefore, the resulting twin vortex becomes asymmetrical. The fringe pattern was generated by the combined effect of the local supersonic flow and the vortices.

## 6.12 Reflection of Transmitted Shock Waves

Installing a splitting plate symmetrically in the 60 mm × 150 mm diaphragm-less shock tube, the evolution of the shock wave diffraction from the splitting plate for Ms = 1.335 in air at 271 hPa, 290.0 K. The plate was set carefully so that the shock wave would diffract precisely symmetrically at the corner of the splitting plate. This experiment was conducted for achieving the intersection of two shock wave having exactly the same strength without having any visible disturbances. As seen in Fig. 6.49, the intersection of the two shock waves forms at first a regular RR and with the increase in the intersecting angle the transition to a MR occur.

### 6.12.1 Head-on Collision of Two Spherical Shock Waves

Two 25 mm diameter shock tubes made of aluminum alloy, were placed to each other at 80 mm stand-off distance and were operated at the identical initial condition. The shock tubes were operated in a synchronized way by rupturing their diaphragms simultaneously. This is achieved by igniting micro-charges.

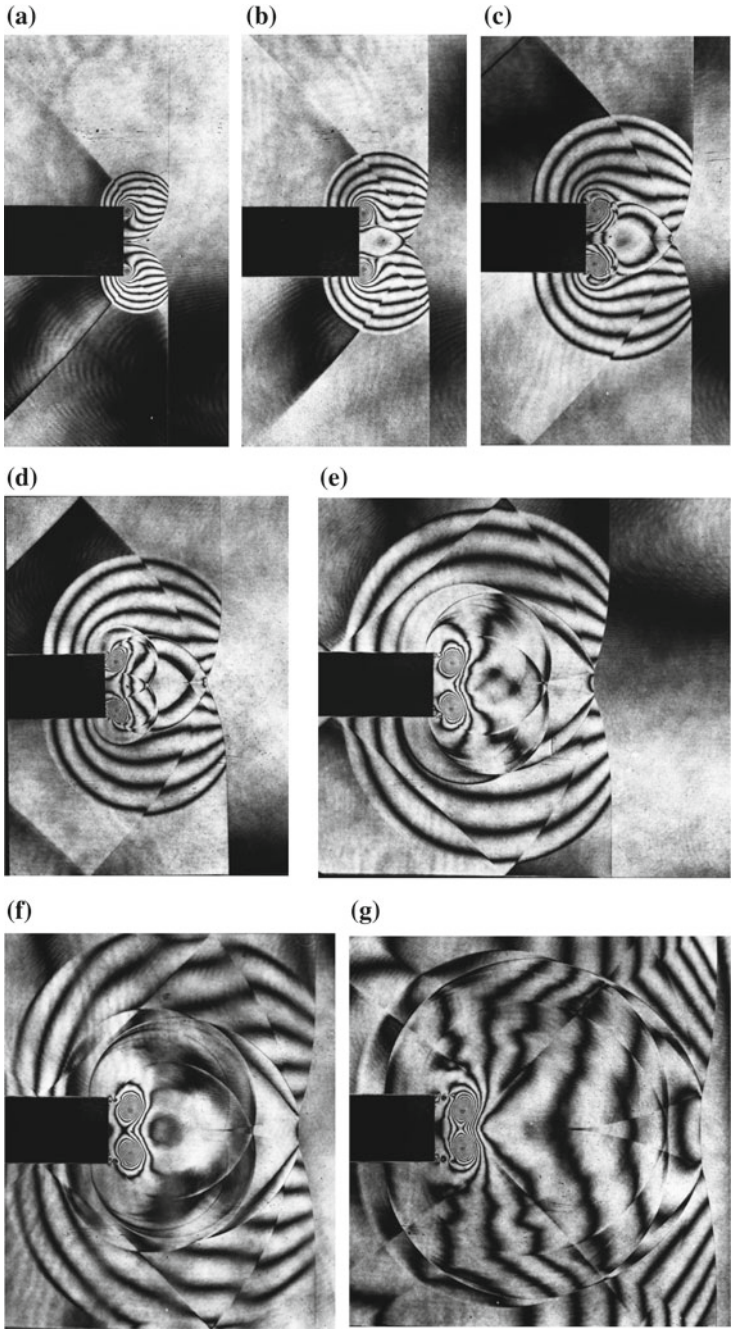


**Fig. 6.47** The evolution of diffraction of the transmitted shock wave at backward facing corner for Ms = 1.24 in atmospheric air at 292.8 K: **a** #87111702, Ms = 1.249; **b** #87111701, Ms = 1.244; **c** #87111703, Ms = 1.244; **d** #87111704, Ms = 1.236; **e** #87111705, Ms = 1.250; **f** #87111706, Ms = 1.243; **g** #87111707, Ms = 1.252

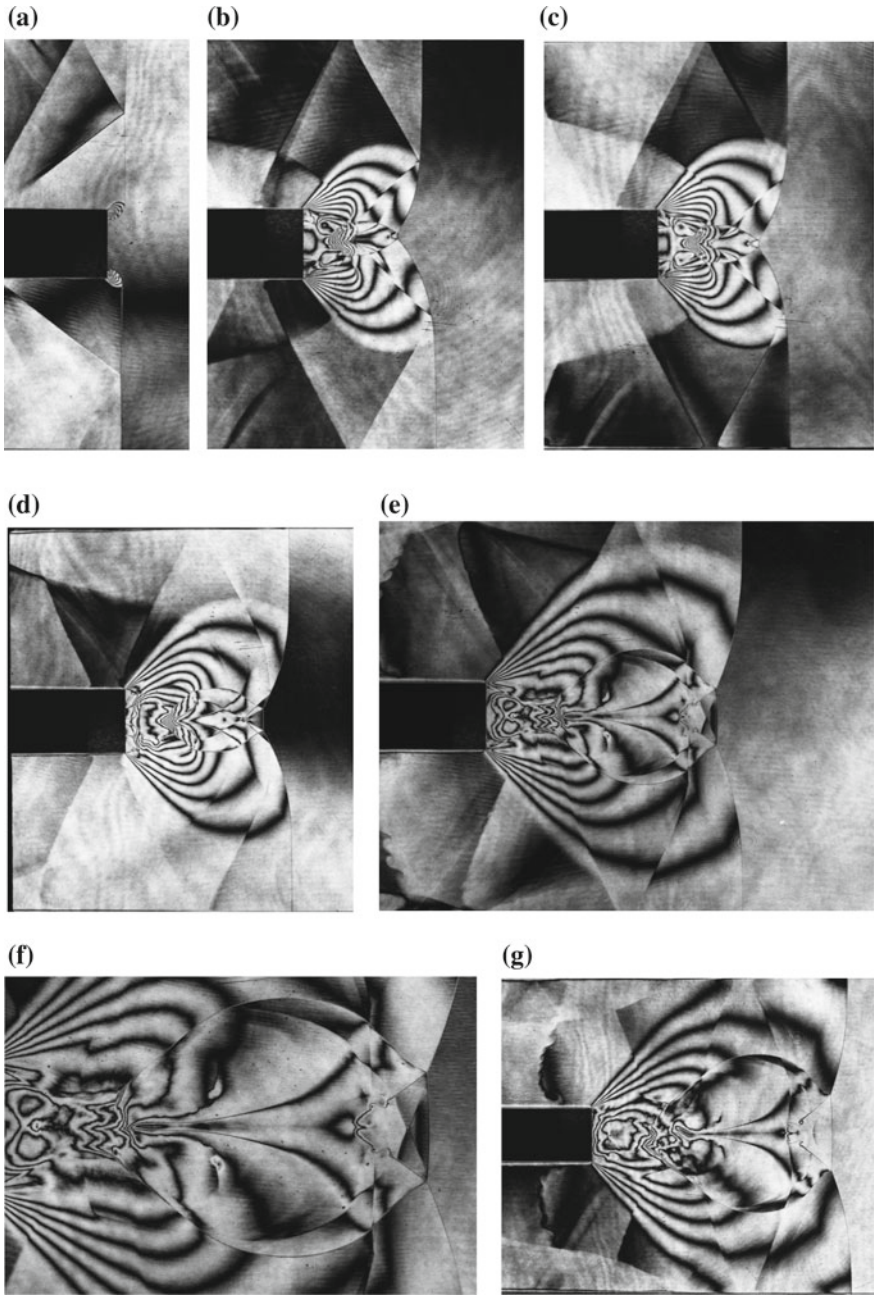


**Fig. 6.48** The evolution of asymmetric interaction of transmitted shock waves from a 50 mm wide splitting plate for Ms = 1.50 in atmospheric air at 294.2 K: **a** #87111713, 390 μs from trigger point Ms = 1.496; **b** #87111714, 400 μs, Ms = 1.471; **c** #87111715, 450 μs, Ms = 1.494; **d** #87111716, 500 μs, Ms = 1.498; **e** #87111717, 520 μs, Ms = 1.501; **f** enlargement of (**e**); **g** #87111718, 540 μs, Ms = 1.501

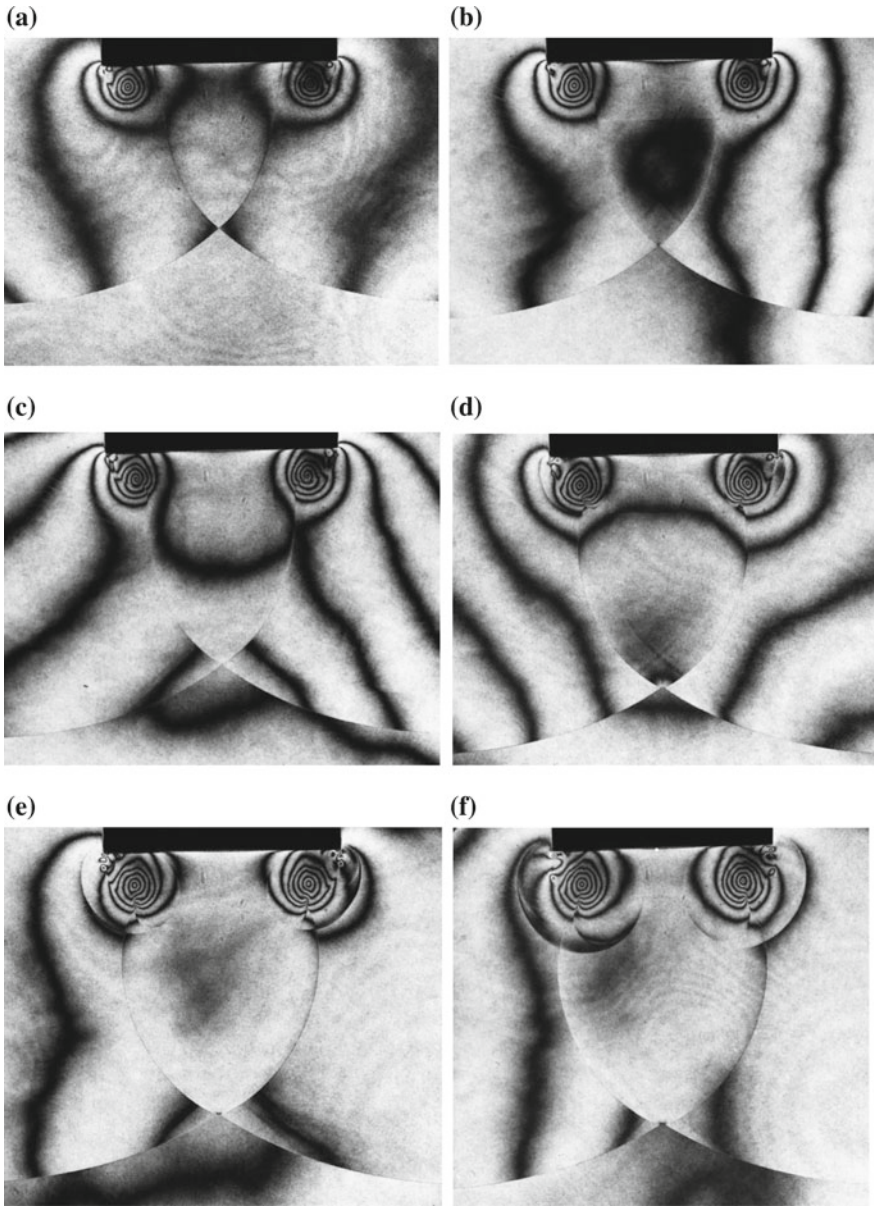


**Fig. 6.49** The interaction of transmitting shock waves for Ms = 1.335 in air at 271 hPa, 290.0 K: **a** #97030301, 550 μs from trigger point Ms = 1.337; **b** #97030302, 575 μs, Ms = 1.33; **c** #97030303, 600 μs, Ms = 1.334; **d** #97030304, 625 μs, Ms = 1.336; **e** #97030305, 650 μs, Ms = 1.335; **f** #97030306, 675 μs, Ms = 1.337; **g** #97031006, 595 μs, Ms = 1.335; **h** #97031008, 600 μs, Ms = 1.339; **i** #97031009, 605 μs, Ms = 1.336; **j** #97031010, 610 μs, Ms = 1.335

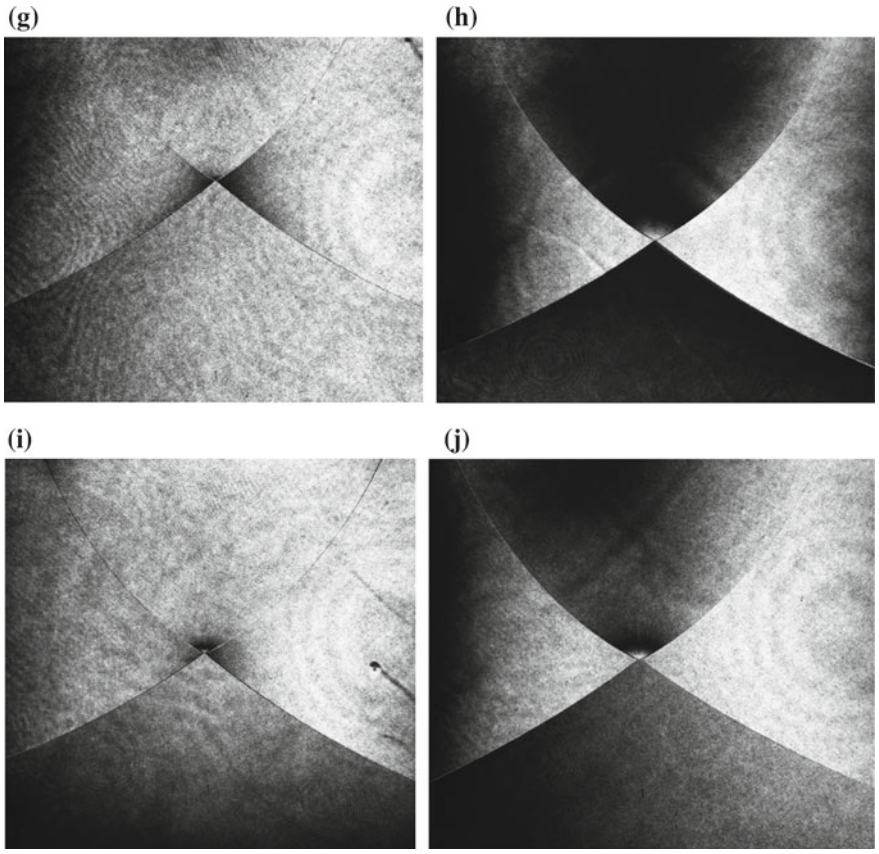


**Fig. 6.49** (continued)

Figure 6.50 show steps in the head-on collision of two spherical shock waves for Ms = 1.22 in atmospheric air at 298 K. The two shock tubes produced shock waves of nearly identical strength. Figure 6.50 show the head-on collision of the two spherical shock waves. The reflection pattern so far observed was a RR.

## 6.13 Effects of Wall Condition on Shock Wave Mitigations

Although it is a laboratory scale experiment from a very narrow-sighted point of view, an effect of wall conditions on the shock wave mitigation was investigated (Abe 2002). Figure 6.51 shows a grassland model placed in the test section of the 60 mm × 150 mm diaphragm-less shock tube. Sequential visualizations were

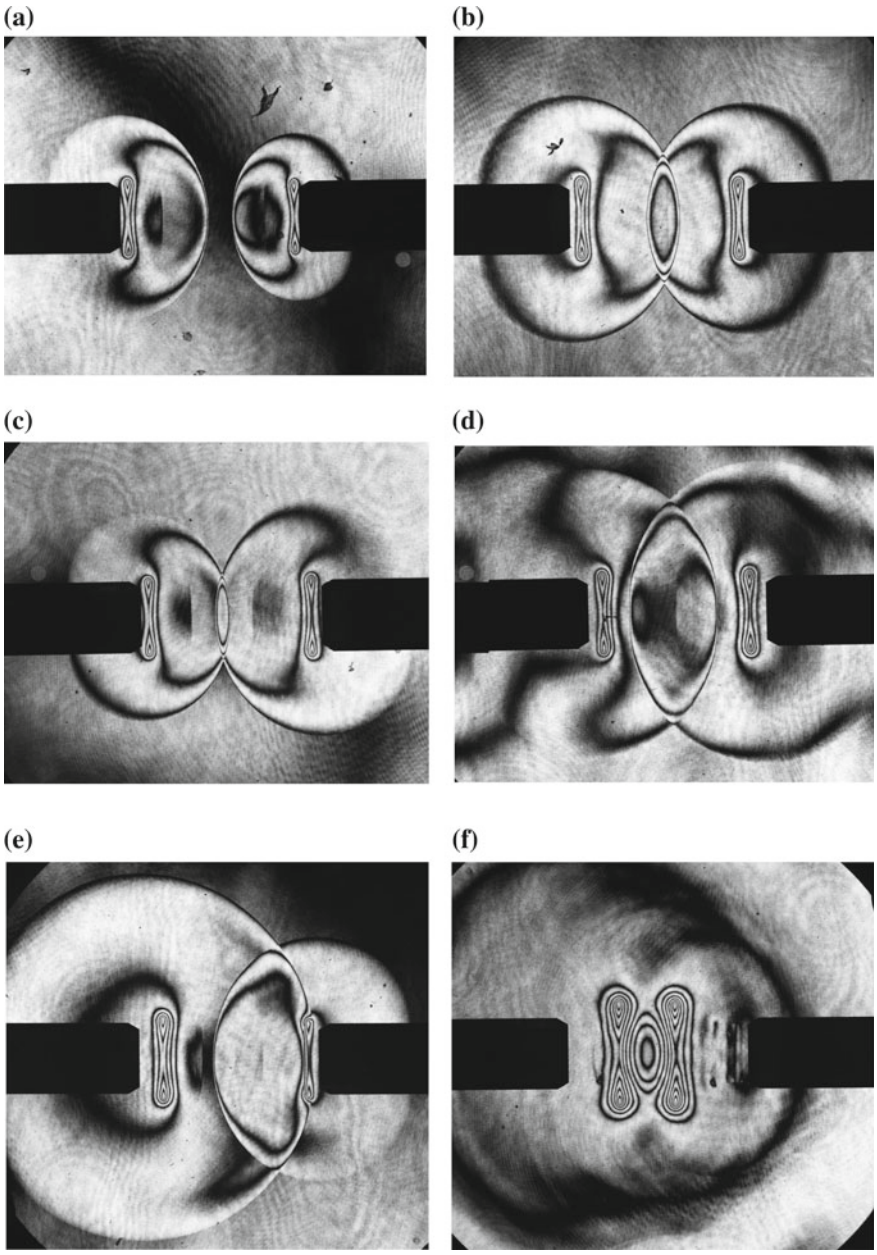


**Fig. 6.50** Reflection of two spherical shock waves released from 25 mm diameter shock tubes separated 80 mm for Ms = 1.22 in atmospheric air at 298 K: **a** #87100911, 3.45 ms delay time from trigger point Ms = 1.233; **b** #87100912, 3.47 ms, Ms = 1.233; **c** #87100907, 3.50 ms, Ms = 1.232; **d** #87100909, 3.52 ms, Ms = 1.245; **e** #87100908, 3.53 ms, Ms = 1.221; **f** #87100905, Ms = 1.233; **g** enlargement of (**b**)

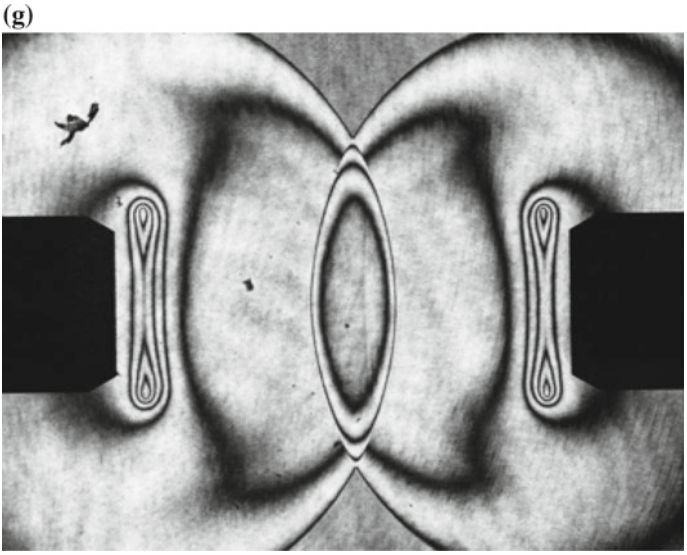


**Fig. 6.50** (continued)

Grassland 60mm × 300mm,10mm height

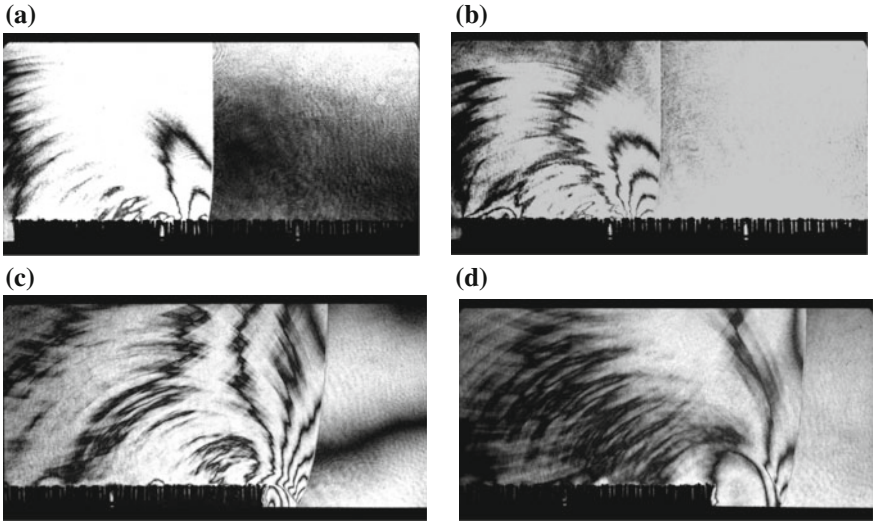


**Fig. 6.51** Simulation of grassland 60 mm × 300 mm, 10 mm in height for Ms = 1.50 at atmospheric air (Abe 2002)

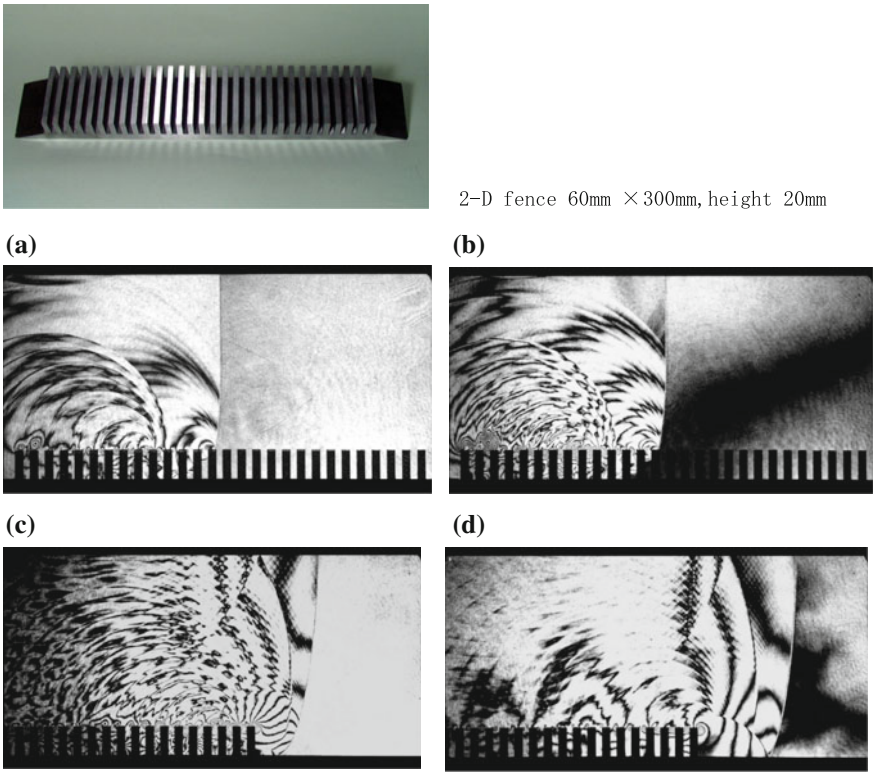


**Fig. 6.52** Simulation of 2-D fence 60 mm × 300 mm, height 20 mm, width 5 mm, pitch 5 mm (Abe 2002)

conducted for Ms = 1.50 in atmospheric air. The grassland model consisted of an artificial turf made of plastic which was expected to move freely at the shock wave loading. Although the turf did moved as seen in Fig. 6.51, the plastic turf move less flexibly than initially expected. Hence, the effet of the grass land on the shock wave mitigation was not significant. If a very soft and flexible plastic turf may be used, the shock wave would be attenuated significantly (Fig. 6.52).

Figure 6.53 shows a 60 mm × 300 mm base made of brass, on which variously shaped fences or objects were installed. Shock waves passing over these obstacles attenuate. The degree of attenuation was more or less similar to the shock wave propagation along compactly distributed I-beams or attenuation along Alporous wall.

Arrayed cones having 15mm base diameter, 30mm high

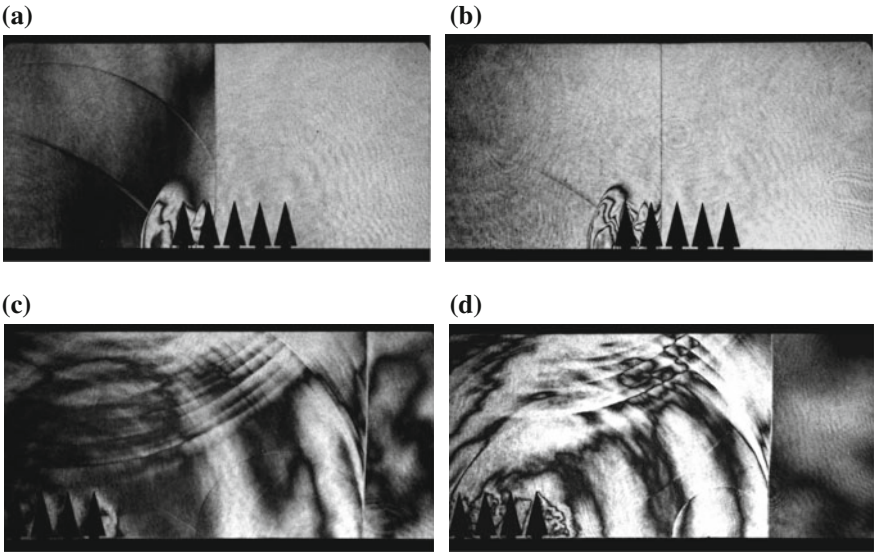


**Fig. 6.53** Arrayed cones having base diameter ϕ15 mm and 30 mm in height for Ms = 1.5 in atmospheric air (Abe 2002)

A shock wave propagation over 25 mm base diameter and 30 mm high cones packed in a 60 mm × 300 mm stand made of brass. The shock Mach number was 1.50 in atmospheric air. Three-dimensional array of cones effectively attenuated the transmitted shock wave by the same physical background that the arrayed spheres mitigated the transmitted shock waves train much more efficiently than the arrayed cylinder did.

Figure 6.54 show sequential observation of arrayed cylinders of 15 mm diameter and 30 mm high and tested for Ms = 1.50 in atmospheric air. The shock wave is attenuated much more effectively than the transmitted shock wave propagation over the two-dimensional slotted wall. The interaction of shock waves with three-dimensionally arrayed cylinders and cones are not investigated well. The efforts of numerical simulation were just started.

Arrayed cylinders, 15mm diameter and 30mm high

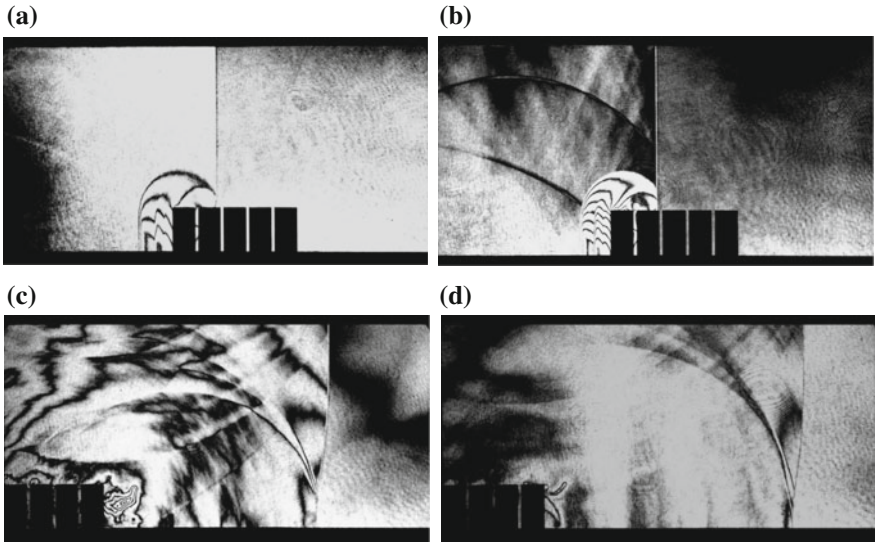


**Fig. 6.54** Arrayed cylinders having ϕ15 mm in diameter and 30 mm in height. Tested for Ms = 1.5 in atmospheric air (Abe 2002)

During a field test of high-explosives, blast waves propagated over a forest. Then the resulting blast wave created a big bang noise. The reflection of the blast wave from the forest was not a startling noise but a noise similar to a sound hundreds of people murmured at the same time. The shock wave reflected from a moving boundary drastically mitigated and became a train of compression waves. This procedure is one of difficult taskes. The experimental result presented in Fig. 6.55 was intended to simulate the shock wave reflection from moving boundaries: 15 mm diameter and 37 mm high rubber tubes arrayed as shown in Fig. 6.55. The experiments were conducted for Ms = 1.5 in atmospheric air.


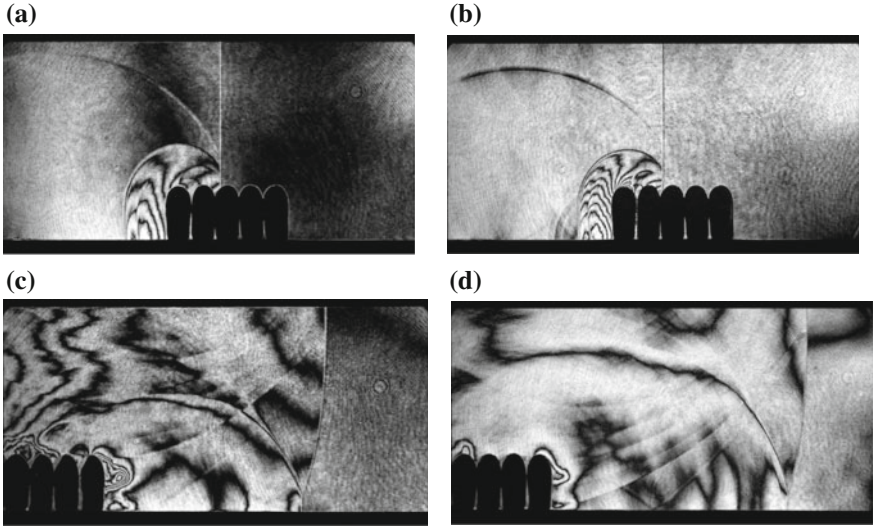


**Fig. 6.55** Arrayed 15 mm diameter and 37 mm high rubber tubes for Ms = 1.5 in atmospheric air (Abe 2002)

## References

Abe, A. (2002). *Experimental and analytical studies of shock wave attenuation over bodies of complex configurations*. (Ph.D. thesis), Graduate School of Engineering, Faculty of Engineering, Tohoku University.

Matsuoka, K. (1997). *Study of mitigation of high speed train tunnel sonic boom*. (Master thesis). Graduate School of Engineering, Faculty of Engineering, Tohoku University.

Matsumura, S. (1995). *Study of automobile exhaust gas induced shock waves and noises*. (Ph.D. thesis), Graduate School of Engineering, Faculty of Engineering, Tohoku University.

Ohtomo, T. (1998). *Study of shock wave attenuation along ducts of complex geometry*. (Master thesis), Graduate School of Engineering, Faculty of Engineering, Tohoku University.

Onodera, H., & Takayama, K. (1990). Shock wave propagation over slitted wedge. *Institute of Fluid Science, Tohoku University, 1,* 45–46.

Sasoh, A., Matsuoka, K., Nakashio, K., Timfeev, E. V., Takayama, K., Voinovich, P. A., et al. (1998). Attenuation of weak shock waves along partially perforated walls. *Shock Waves, 8,* 149–159.

Sekine, N., Matsumura, S., Aoki, K., & Takayama, K. (1989). Generation and propagation of shock waves in the exhaust pipe of a four cycle automobile engine. In Y. W. Kim (Ed.), *Current Topics in Shock Waves, Proceedings of 17th International Symposium on Shock Tubes and Shock Waves*, Bethlehem (pp. 671–676).

Takayama, K. (1993). Optical flow visualization of shock wave phenomena In R. Brun & L. Z. Dumitrescu (Eds.), *Proceedings of 19th ISSW* (Vol. 4, pp. 7–17). Marseille.

Voinovich, P. A., Timofeev, E. V., Saito, T., & Takayama, K. (1998). Supercomputer simulation of 3-D unsteady gas flows using a locally adoptive unstructured grid techniques. In *Proceedings of 16th International Conference on Numerical Method in Fluid Dynamics* (pp. 51–52).